

# Signatures of indirect $K$ -edge resonant inelastic x-ray scattering on magnetic excitations in a triangular-lattice antiferromagnet

Cheng Luo,<sup>1</sup> Trinanjan Datta,<sup>2,\*</sup> Zengye Huang,<sup>1</sup> and Dao-Xin Yao<sup>1,†</sup><sup>1</sup>*State Key Laboratory of Optoelectronic Materials and Technologies, School of Physics and Engineering, Sun Yat-Sen University, Guangzhou 510275, China*<sup>2</sup>*Department of Chemistry and Physics, Georgia Regents University, 1120 15th Street, Augusta, Georgia 30912, USA*

(Received 27 April 2015; revised manuscript received 18 June 2015; published 6 July 2015)

We compute the  $K$ -edge indirect resonant inelastic x-ray scattering (RIXS) spectrum of a triangular-lattice antiferromagnet in its ordered coplanar three-sublattice  $120^\circ$  magnetic state. By considering the self-energy corrections to the spin-wave spectrum, magnon decay rates, bimagnon interactions within the ladder approximation Bethe-Salpeter scheme, and the effect of three-magnon contributions up to  $1/S$  order, we find that the RIXS spectra are nontrivially affected by magnon damping and anisotropy. For a purely isotropic model, the appearance of a multipeak RIXS structure is primarily dictated by the damping of magnon modes. A unique feature of the triangular-lattice indirect RIXS spectra is the nonvanishing intensity at both the zone center  $\Gamma$  point and the antiferromagnetic wave-vector  $K$  point. Additionally, we find that a single-peak RIXS spectrum forms at the roton momentum which can be utilized as an experimental signature to detect the presence of rotonlike excitations. However, including  $XXZ$  anisotropy leads to additional peak splitting, including at the roton wave vector. The observed splitting is consistent with our earlier theoretical prediction on the effects of spatial anisotropy on the RIXS spectra of a frustrated quantum magnet [C. Luo, *et al.*, *Phys. Rev. B* **89**, 165103 (2014)].

DOI: [10.1103/PhysRevB.92.035109](https://doi.org/10.1103/PhysRevB.92.035109)

PACS number(s): 78.70.Ck, 75.25.-j, 75.10.Jm

## I. INTRODUCTION

Contrary to the historical prediction of the spin- $\frac{1}{2}$  triangular-lattice antiferromagnet (TLAF) as a canonical example of a spin-liquid state [1], extensive theoretical [2–4], numerical [5–11], and experimental [12–20] studies on the nearest-neighbor Heisenberg model have established the ground-state configuration as a  $120^\circ$  long-range coplanar three-sublattice arrangement. The predicted ordering pattern persists for all values of spin  $S$ , including the  $S = \frac{1}{2}$  state where quantum fluctuations lead to a 60% suppression of the magnetic order parameter from its classical Néel value [5–8]. At present there exists a plethora of real TLAF materials, with both isotropic and anisotropic interactions, which provide a motivation to study triangular-lattice frustrated magnets [12,15–21]. Further impetus to investigate and delineate the physical properties of the TLAF stems from the flurry of recent theoretical and numerical investigations to clarify the ground- and excited-state properties of both isotropic and anisotropic triangular-lattice systems [22–31].

Traditionally, information on the magnetic ground state and single-magnon excitations is inferred from inelastic neutron scattering (INS) experiments [32,33]. However, with enhancements in instrumental resolution of the next-generation synchrotron radiation sources resonant inelastic x-ray scattering (RIXS) spectroscopy offers the condensed-matter and materials science community an alternate option to experimentally probe magnetic excitations in correlated magnets [34]. As a *photon-in, photon-out* spectroscopic technique, RIXS can offer direct information on both single-magnon and multi-magnon excitations. Present efforts to understand the  $K$ -edge

indirect RIXS spectra are primarily directed towards the study of square-lattice compounds in the Néel antiferromagnetic and collinear antiferromagnetic phases [35–41]. In a recent publication [40], the authors of this paper have shown that in the case of an anisotropic square lattice with strong frustrating farther-neighbor interactions the RIXS spectrum can split into a robust two-peak structure over a wide range of transferred momenta in both magnetically ordered phases. It was also predicted that the unfrustrated model contains a single-peak structure.

In RIXS spectroscopy single- and three-spin-flip processes are allowed at the  $L$  and  $M$  edges due to the presence of spin-orbit coupling [42–45]. But in a square lattice, excitations of odd magnons are prohibited at the  $K$  edge [34], and the spectra originate purely from the bimagnon contribution. In the absence of an external magnetic field the spin ordering in a square-lattice system is collinear, and the magnon excitations are long-lived without any damping. In contrast, in the TLAF the noncollinear ground state contains inherent three-magnon excitations (odd spin-flip terms). The coupling of the longitudinal and transverse spin excitations gives rise to the finite quasiparticle lifetime (see Fig. 1), which introduces an intrinsic damping of the magnon modes [46,47]. Hence, the presence of the trimagnon interaction, even at the  $K$  edge, motivates several unanswered questions within the context of quantum magnetism and RIXS spectroscopy. How does the presence of an intrinsic damping affect the indirect  $K$ -edge RIXS spectra? What role does the interplay between geometrical frustration and spin anisotropy have on the RIXS spectra? In this paper, we predict the effects of bimagnon and trimagnon processes in indirect RIXS spectroscopy of a geometrically frustrated TLAF, a topic which is unexplored both theoretically and experimentally.

The microscopic mechanism underlying magnetic excitations in the indirect RIXS process involves a local modification

\*Corresponding author: [tdatta@gru.edu](mailto:tdatta@gru.edu)†Corresponding author: [yaodaox@mail.sysu.edu.cn](mailto:yaodaox@mail.sysu.edu.cn)

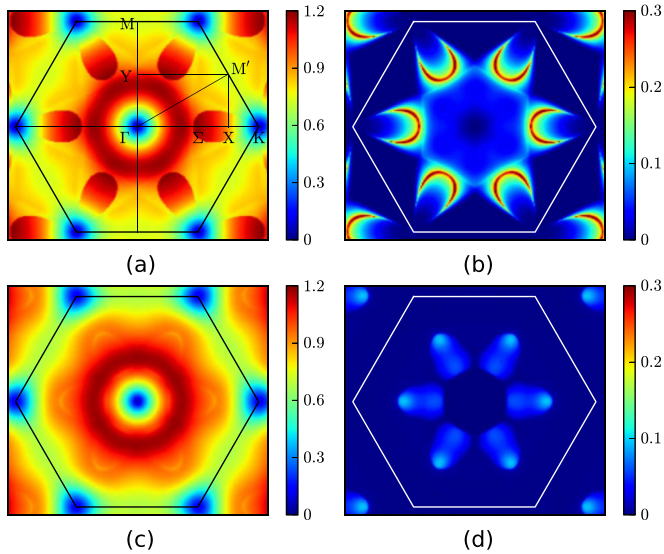


FIG. 1. (Color online) Intensity maps of the  $1/S$  spin-wave spectrum for the  $S = 1/2$  triangular-lattice antiferromagnet with (top) easy-plane anisotropy  $\alpha = 1$  and (bottom)  $\alpha = 0.95$ . (a) and (c) Renormalized magnon energy  $\tilde{\omega}_k$ . (b) and (d) Magnon decay rate  $\Gamma_k$ .  $\Gamma = (0,0)$ ,  $\Sigma = (2\pi/3,0)$ ,  $X = (\pi,0)$ ,  $K = (4\pi/3,0)$ ,  $M = (0,2\pi/\sqrt{3})$ , and  $Y = (0,\pi/\sqrt{3})$  points in (a) are highlighted. Note the overall damping of spin waves is strongly reduced, and the decay region shrinks with increasing anisotropy. The realistic magnon decays disappear at  $\alpha \approx 0.92$  [56].

of the superexchange interaction mediated via the core hole [48,49]. The resulting RIXS spectrum is expressed as a momentum-dependent four-spin correlation function which can probe bimagnon excitations across the entire Brillouin zone (BZ) [37–39]. Hence, RIXS is complementary to optical Raman scattering, which is restricted to zero momentum [50–53]. From a theoretical perspective elucidating the nature of the bimagnon dispersion affected by both two-magnon ladder scattering processes and three-magnon interactions is challenged by the appearance of several nontrivial dynamical properties in the spin-wave excitation spectrum [47,54–56]. Namely, (i) strong renormalization of magnon energies with respect to the linear spin-wave theory result, (ii) finite lifetime due to spontaneous magnon decays at zero temperature, and (iii) the appearance of rotonlike minima at the edge center of the BZ [ $M$  point; see Fig. 1(a)].

The objective of this paper is to elucidate the role of magnon-magnon interaction, spontaneous magnon decays, the effect of the rotonlike minima, and spin anisotropy on the indirect RIXS spectra of a TLAF. For this purpose, we consider an easy-plane  $XXZ$  triangular-lattice model. In the isotropic limit, the  $XXZ$  model can provide an accurate description of the  $\text{Ba}_3\text{CoSb}_2\text{O}_9$  system [12,57]. In addition, it provides a starting point for the discussion of RIXS effects in anisotropic TLAF [15–20]. We compute the RIXS intensity utilizing the  $1/S$  spin-wave expansion technique within the Bethe-Salpeter scheme in which interaction effects arising from both the quartic terms via the ladder scattering process and the contributions of the cubic anharmonic terms up to  $1/S$  order are included.

The main results of our paper can be summarized as follows. First, in the case of an isotropic nearest-neighbor TLAF we find that the spontaneous magnon decay and kinematic constraints of the phase space inherent to the model are the primary cause for the creation of a multipeak (more than two-peak) structure in the RIXS spectra. Second, contrary to the  $K$ -edge RIXS intensity of the square-lattice case, in the TLAF the RIXS intensity does not vanish at the  $\Gamma$  point and at the  $K$  point. At the  $\Gamma$  point, the bimagnon intensity is zero, and the single-peak spectrum results purely from the trimagnon contribution, approximately at energy scale of  $6JS$  corresponding to the three-magnon energy. This provides experimentalists with a means to detect purely trimagnon excitations at the  $K$  edge. At the antiferromagnetic wave vector  $K$  point the RIXS intensity is dominated by the bimagnon excitations. Third, an important conclusion of our work is the proposal of utilizing RIXS as a probe to detect the presence of the roton mode. We show that at a scattering wave vector equal to the roton momentum  $\mathbf{q} = M$  the RIXS spectrum has a single-peak structure. Barring the  $\Gamma$  point peak which occurs at higher energy, at all other special high-symmetry points of the magnetic BZ the RIXS spectra split into a multipeak structure. The appearance of the single-peak structure can serve as an experimental signature to detect the appearance of a roton mode in a TLAF. Fourth, including the  $XXZ$  anisotropy leads to further peak splitting including at the roton scattering wave vector. Fifth, we find that the conceptual signature of slow-moving bimagnons as an indicator of RIXS peak splitting (instability), as proposed in our earlier work on the two-peak splitting theory within the context of the anisotropic square-lattice Heisenberg model [40], still holds (see Fig. 8 below).

This paper is organized as follows. In Sec. II, we introduce the  $XXZ$  model, present the expression for the effective bosonic Hamiltonian within an interacting spin-wave formalism, and compute the intensity maps for the renormalized energy and magnon decay rate, up to  $1/S$  corrections. In Sec. III, we state the definition and the expression of the TLAF RIXS scattering operator containing both the bimagnon and trimagnon contributions. In Sec. IV, we display our results, state the formalism and numerical approach for computing RIXS intensity, and discuss the implications of our result within the context of a TLAF (geometric frustration). First, in Sec. IV A, we present the results for the noninteracting bimagnon and trimagnon RIXS intensity and spectral weight. In Sec. IV B, we outline our formalism and calculate the interacting bimagnon intensity. In Sec. IV C, we calculate the full RIXS spectrum. In Sec. V, we present our concluding remarks and discuss the appearance of slow-moving bimagnons as a signature of peak splitting. Finally, to preserve clarity in the main body of the text, we state the details of the spin-wave-theory derivation of the effective Hamiltonian in Appendix A and display results to validate our numerical approach in Appendix B.

## II. TLAF MODEL AND MAGNON DECAY

INS data of a TLAF reveal well-defined sharp modes in the low-energy excitation spectrum accompanied by a broad continuum at intermediate and high energies [57–59]. A number of competing theoretical proposals, ranging from

a proximate spin-liquid phase [25,28] to enhanced magnon-magnon interactions [60–62], have been proposed to explain the nature of the spin-wave excitation spectrum. Our starting point is the spin  $S$ , nearest-neighbor  $XXZ$  antiferromagnetic model on the triangular lattice. The spin-wave-theory Hamiltonian in the local  $(x-z)$  rotating frame associated with the ordering wave vector  $\mathbf{Q} = (4\pi/3, 0)$ , the  $K$  point in the BZ, takes the following form [56]:

$$\mathcal{H} = J \sum_{\langle ij \rangle} [\alpha S_i^y S_j^y + \cos(\theta_i - \theta_j)(S_i^z S_j^z + S_i^x S_j^x) + \sin(\theta_i - \theta_j)(S_i^z S_j^x - S_i^x S_j^z)], \quad (1)$$

where  $\theta_i = \mathbf{Q} \cdot \mathbf{r}_i$  and we have also introduced an easy-plane anisotropy parameter  $\alpha \in [0, 1]$ . In Appendix A we outline the derivation of the effective interacting spin-wave Hamiltonian  $\mathcal{H}_{\text{eff}}$  in the first-order  $1/S$  expansion with respect to linear spin-wave theory. The resulting expression is

$$\mathcal{H}_{\text{eff}} = \sum_{\mathbf{k}} (\varepsilon_{\mathbf{k}} + \delta\varepsilon_{\mathbf{k}}) b_{\mathbf{k}}^\dagger b_{\mathbf{k}} + \frac{1}{2!} \sum_{\{\mathbf{k}_i\}} V_a (b_1^\dagger b_2^\dagger b_3 + \text{H.c.}) + \frac{1}{3!} \sum_{\{\mathbf{k}_i\}} V_b (b_1^\dagger b_2^\dagger b_3^\dagger + \text{H.c.}) + \sum_{\{\mathbf{k}_i\}} V_c b_1^\dagger b_2^\dagger b_3 b_4, \quad (2)$$

where  $b^\dagger$  ( $b$ ) is the magnon creation (annihilation) operator and we have adopted the convention that  $1 = \mathbf{k}_1, 2 = \mathbf{k}_2$ , etc., with momentum conservation being assumed for various  $\mathbf{k}$  summations. The bare magnon dispersion given by the linear spin-wave theory is expressed as

$$\varepsilon_{\mathbf{k}} = 3JS\sqrt{(1 - \gamma_{\mathbf{k}})(1 + 2\alpha\gamma_{\mathbf{k}})}, \quad (3)$$

with  $\gamma_{\mathbf{k}} = \frac{1}{3}[\cos k_x + 2\cos(k_x/2)\cos(\sqrt{3}k_y/2)]$ . The explicit forms for the interacting vertices  $\delta\varepsilon$ ,  $V_{a,b}$ , and  $V_c$  are detailed in Appendix A. At zero temperature the bare magnon propagator is defined as

$$G_0^{-1}(\mathbf{k}, \omega) = \omega - \varepsilon_{\mathbf{k}} + i0^+. \quad (4)$$

The first-order  $1/S$  correction to the magnon energy is determined by the Dyson equation

$$\omega - \varepsilon_{\mathbf{k}} - \Sigma(\mathbf{k}, \omega) = 0, \quad (5)$$

with the one-loop self-energy  $\Sigma(\mathbf{k}, \omega) = \Sigma_a(\mathbf{k}, \omega) + \Sigma_b(\mathbf{k}, \omega) + \Sigma_c(\mathbf{k})$ , where  $\Sigma_c(\mathbf{k}) = \delta\varepsilon_{\mathbf{k}}$  is a frequency-independent Hartree-Fock correction, while  $\Sigma_{a,b}(\mathbf{k}, \omega)$  are calculated as [4,47,55,56]

$$\Sigma_a(\mathbf{k}, \omega) = \frac{1}{2} \sum_{\mathbf{p}} \frac{|V_a(\mathbf{p}, \mathbf{k} - \mathbf{p}; \mathbf{k})|^2}{\omega - \varepsilon_{\mathbf{p}} - \varepsilon_{\mathbf{k}-\mathbf{p}} + i0^+}, \quad (6)$$

$$\Sigma_b(\mathbf{k}, \omega) = -\frac{1}{2} \sum_{\mathbf{p}} \frac{|V_b(\mathbf{p}, -\mathbf{k} - \mathbf{p}, \mathbf{k})|^2}{\omega + \varepsilon_{\mathbf{p}} + \varepsilon_{\mathbf{k}+\mathbf{p}} - i0^+}. \quad (7)$$

The on-shell solution consists of setting  $\omega = \varepsilon_{\mathbf{k}}$  in the self-energy (6), and (7) leads to the following expression for the  $1/S$  renormalized spectrum:

$$\omega_{\mathbf{k}} \equiv \bar{\omega}_{\mathbf{k}} - i\Gamma_{\mathbf{k}} = \varepsilon_{\mathbf{k}} + \Sigma(\mathbf{k}, \varepsilon_{\mathbf{k}}), \quad (8)$$

where  $\bar{\omega}_{\mathbf{k}} = \text{Re}[\omega_{\mathbf{k}}]$  is the renormalized spin-wave energy and  $\Gamma_{\mathbf{k}} = -\text{Im}[\omega_{\mathbf{k}}]$  represents the magnon decay rate. In Fig. 1 we

display the intensity maps for  $\bar{\omega}_{\mathbf{k}}$  and  $\Gamma_{\mathbf{k}}$  scaled by  $3JS$  for the  $S = 1/2$  triangular antiferromagnet with  $\alpha = 1$  (isotropic) and  $\alpha = 0.95$  (anisotropic). From Fig. 1(d) we observe that the magnon decay rate decreases drastically in the presence of anisotropy. This is due to the reduced phase volume where the kinematic constraint  $\varepsilon_{\mathbf{k}} = \varepsilon_{\mathbf{p}} - \varepsilon_{\mathbf{k}-\mathbf{p}}$  in the self-energy (6) is satisfied. The magnon decay intensity maps in Figs. 1(b) and 1(d) play an important role in our understanding of the origins of the multipeak RIXS structure (shown in Figs. 6 and 7 below).

### III. INDIRECT RIXS CORRELATOR

In Mott-insulating systems, multimagnon excitations can be created dynamically by the presence of the core-hole potential in the intermediate state of indirect RIXS process. The effective scattering operator, in the first order, under the assumption of the ultrashort core-hole lifetime (UCL) expansion is given by [37,39]

$$\mathcal{R}_{\mathbf{q}} = J \sum_{i, \delta} e^{i\mathbf{q} \cdot \mathbf{r}_i} \mathbf{S}_i \cdot \mathbf{S}_{i+\delta}, \quad (9)$$

where  $\mathbf{r}_i$  is the position of the ion absorbing the incident photon and  $\delta$  denotes the neighboring vectors. After consecutive Holstein-Primakoff and Bogoliubov transformations, the magnon creation parts of the RIXS scattering operator can be expressed in terms of the bosonic operators as

$$\mathcal{R}_{\mathbf{q}} = \sum_{1+2=\mathbf{q}} M(1,2) b_1^\dagger b_2^\dagger + \sum_{1+2+3=\mathbf{q}} N(1,2,3) b_1^\dagger b_2^\dagger b_3^\dagger, \quad (10)$$

where the bimagnon scattering matrix element expression is given by

$$M(1,2) = \frac{3JS}{2!} \left\{ \left[ 1 + \gamma_{\mathbf{q}} + \left( \alpha - \frac{1}{2} \right) (\gamma_1 + \gamma_2) \right] (u_1 v_2 + v_1 u_2) - \left( \alpha + \frac{1}{2} \right) (\gamma_1 + \gamma_2) (u_1 u_2 + v_1 v_2) \right\}, \quad (11)$$

and the trimagnon scattering matrix element is given by

$$N(1,2,3) = \frac{3JS}{3!} i \sqrt{\frac{3}{2S}} \left[ \left( \bar{\gamma}_1 - \bar{\gamma}_{2+3} - \frac{1}{4} \bar{\gamma}_{\mathbf{q}} \right) (u_1 + v_1) \times (u_2 v_3 + v_2 u_3) + \left( \bar{\gamma}_2 - \bar{\gamma}_{1+3} - \frac{1}{4} \bar{\gamma}_{\mathbf{q}} \right) (u_2 + v_2) \times (u_1 v_3 + v_1 u_3) + \left( \bar{\gamma}_3 - \bar{\gamma}_{1+2} - \frac{1}{4} \bar{\gamma}_{\mathbf{q}} \right) (u_3 + v_3) \times (u_1 v_2 + v_1 u_2) \right], \quad (12)$$

where  $u$ ,  $v$ , and  $\bar{\gamma}$  are defined in Appendix A. The three-boson term in our theory has no analog in the collinear phases of a square-lattice quantum magnet. Note that the corrections from magnon interactions for the trimagnon intensity appear at the  $1/S^2$  order and are neglected in the remainder of this paper.

The frequency- and momentum-dependent magnetic scattering intensity is related to the multimagnon response function via the fluctuation-dissipation theorem. The full  $1/S$  correction

to the indirect RIXS susceptibility is the sum of bimagnon and trimagnon contributions given by

$$\begin{aligned} I(\mathbf{q}, \omega) &= -\frac{1}{\pi} \text{Im}[\chi_2(\mathbf{q}, \omega) + \chi_3(\mathbf{q}, \omega)] \\ &= -\frac{1}{\pi} \text{Im}[\chi_{\text{RIXS}}(\mathbf{q}, \omega)], \end{aligned} \quad (13)$$

which involve an interacting two-magnon susceptibility  $\chi_2(\mathbf{q}, \omega)$  and a noninteracting three-magnon susceptibility  $\chi_3(\mathbf{q}, \omega)$ . The susceptibilities can be expressed explicitly from the corresponding multimagnon Green's function defined as

$$\chi_2(\mathbf{q}, \omega) = \sum_{\mathbf{k}\mathbf{k}'} M_{\mathbf{k}} M_{\mathbf{k}'} \Pi_{\mathbf{k}\mathbf{k}'}(\mathbf{q}, \omega), \quad (14)$$

$$\chi_3(\mathbf{q}, \omega) = \sum_{\mathbf{k}\mathbf{p}; \mathbf{k}'\mathbf{p}'} N_{\mathbf{k}, \mathbf{p}} N_{\mathbf{k}', \mathbf{p}'} \Lambda_{\mathbf{k}\mathbf{p}; \mathbf{k}'\mathbf{p}'}(\mathbf{q}, \omega), \quad (15)$$

where  $\Pi$  and  $\Lambda$  are denoted as the bimagnon and trimagnon propagators, respectively. The momentum-dependent two-magnon and three-magnon Green's functions in terms of Bogoliubov quasiparticles are defined as

$$i \Pi_{\mathbf{k}\mathbf{k}'}(\mathbf{q}, t) = \langle \mathcal{T} b_{\mathbf{k}+\mathbf{q}}(t) b_{-\mathbf{k}}(t) b_{\mathbf{k}'+\mathbf{q}}^\dagger b_{-\mathbf{k}'}^\dagger \rangle, \quad (16)$$

$$i \Lambda_{\mathbf{k}\mathbf{p}; \mathbf{k}'\mathbf{p}'}(\mathbf{q}, t) = \langle \mathcal{T} b_{\mathbf{k}}(t) b_{\mathbf{q}-\mathbf{k}-\mathbf{p}}(t) b_{\mathbf{p}}(t) b_{\mathbf{k}'}^\dagger b_{\mathbf{q}-\mathbf{k}'-\mathbf{p}'}^\dagger b_{\mathbf{p}'}^\dagger \rangle, \quad (17)$$

where  $\mathcal{T}$  is the time-ordering operator and  $\langle \cdot \rangle$  is the average of the ground state. In the following sections, using Eqs. (16) and (17), we will compute the noninteracting and the interacting RIXS spectra.

## IV. RESULTS AND DISCUSSION

### A. Noninteracting bi- and trimagnon spectra

Using Eqs. (11) and (12) and applying Wick's theorem to Eqs. (16) and (17), we obtain the following expressions for the noninteracting bimagnon [ $I_2(\mathbf{q}, \omega)$ ] and trimagnon [ $I_3(\mathbf{q}, \omega)$ ] scattering intensities:

$$I_2(\mathbf{q}, \omega) = 2 \sum_{\mathbf{k}} M_{\mathbf{k}+\mathbf{q}, -\mathbf{k}}^2 \delta(\omega - \varepsilon_{\mathbf{k}+\mathbf{q}} - \varepsilon_{\mathbf{k}}), \quad (18)$$

$$I_3(\mathbf{q}, \omega) = 6 \sum_{\mathbf{k}, \mathbf{p}} N_{\mathbf{k}, \mathbf{q}-\mathbf{k}-\mathbf{p}, \mathbf{p}}^2 \delta(\omega - \varepsilon_{\mathbf{k}} - \varepsilon_{\mathbf{q}-\mathbf{k}-\mathbf{p}} - \varepsilon_{\mathbf{p}}). \quad (19)$$

In Fig. 2, we show the results for the  $S = 1/2$  isotropic Heisenberg model ( $\alpha = 1$ ) at various points in the BZ. At the  $\Gamma$  point the contribution is purely from the trimagnon excitations [see Fig. 2(a)]. The bimagnon RIXS intensity displays a nonzero elastic peak at the  $K$  point [see Fig. 2(f)]. The indirect RIXS spectra even at the noninteracting level in a noncollinear quantum magnet exhibit significant differences from the collinear ordered quantum magnets where the intensity vanishes at the BZ center and at the antiferromagnetic wave vector [37–40]. This statement holds true even in the case of the  $XXZ$  TLAF. The noninteracting bimagnon RIXS intensity in Eq. (18) is proportional to the bare two-magnon density of states (DOS),

$$D_2(\mathbf{q}, \omega) = \sum_{\mathbf{k}} \delta(\omega - \varepsilon_{\mathbf{k}+\mathbf{q}} - \varepsilon_{\mathbf{k}}). \quad (20)$$

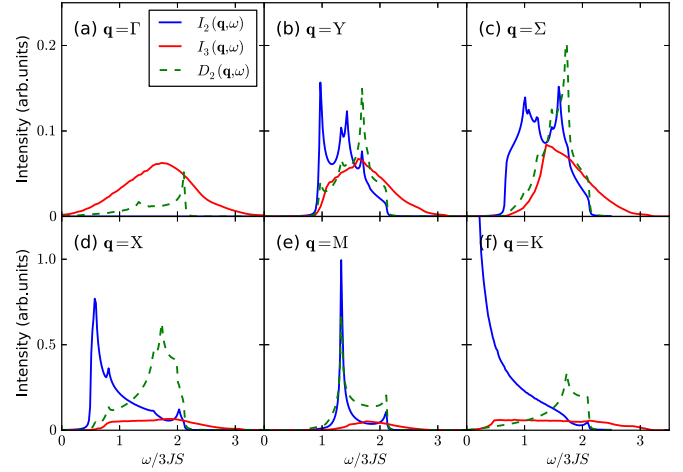


FIG. 2. (Color online) Noninteracting bimagnon [ $I_2(\mathbf{q}, \omega)$ ] and trimagnon [ $I_3(\mathbf{q}, \omega)$ ] RIXS intensity of the isotropic TLAF at momentum transfer  $\mathbf{q}$  corresponding to the special high-symmetry points of a triangular-lattice BZ. The bimagnon DOS  $D_2(\mathbf{q}, \omega)$  is also shown as a dashed line. The nonzero intensity at the  $\Gamma$  and  $K$  points is a unique RIXS feature of the noncollinear ground-state configuration.

A close inspection of the DOS in Fig. 2 shows that these Van Hove singularities, which originate from the maximum or saddle points of the two-magnon continuum  $\varepsilon_{\mathbf{k}+\mathbf{q}} + \varepsilon_{\mathbf{k}}$ , partially transfer to the RIXS intensity [see Figs. 2(b)–2(e)], and the spectrum line shape at  $\mathbf{q} = M$  [Fig. 2(e)] resembles the DOS with minimal RIXS matrix element effects.

In Fig. 3 we show the variation of the total spectral weight across the BZ for the bimagnon [ $\mathcal{S}_2(\mathbf{q})$ ] and trimagnon [ $\mathcal{S}_3(\mathbf{q})$ ] components. By using the bare intensity equations (18) and (19) we obtain

$$\mathcal{S}_2(\mathbf{q}) = \int_0^\infty d\omega I_2(\mathbf{q}, \omega) = 2 \sum_{\mathbf{k}} M^2(\mathbf{k} + \mathbf{q}, -\mathbf{k}), \quad (21)$$

$$\mathcal{S}_3(\mathbf{q}) = \int_0^\infty d\omega I_3(\mathbf{q}, \omega) = 6 \sum_{\mathbf{k}} N^2(\mathbf{k}, \mathbf{q} - \mathbf{k} - \mathbf{p}; \mathbf{p}). \quad (22)$$

In general, the trimagnon excitation dominates the indirect RIXS total spectral weight in the vicinity of the BZ center, while the bimagnon spectral weight becomes overwhelmingly large at the boundary of the BZ where the three-magnon intensity is negligible. The most remarkable feature of the isotropic model [see Fig. 3(a)] is the elastic peak at the antiferromagnetic wave vector which resembles the longitudinal dynamic structure factor probed by neutron-scattering experiments [62–64]. Upon inclusion of anisotropy,  $\alpha = 0.95$ , the elastic peak at  $\mathbf{q} = K$  disappears [see Fig. 3(b)] since a gap is now introduced in the spin-wave dispersion equation (3) at the ordering wave vector.

In Fig. 4 we show the pure trimagnon contribution along the  $\Gamma \rightarrow M$  path obtained using the noninteracting three-magnon susceptibility  $\chi_3(\mathbf{q}, \omega)$  in Eq. (15). We plot the spectra both in the presence and in the absence of anisotropy. We observe that the trimagnon spectra peak occurs at a higher energy approximately around  $6JS$  around the  $\Gamma$  point, which downshifts

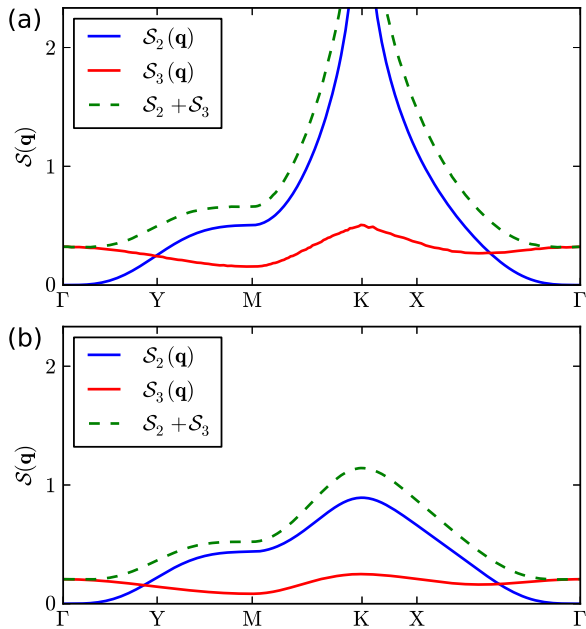


FIG. 3. (Color online) The noninteracting bimagnon and trimagnon total spectral weight for (a) isotropic ( $\alpha = 1$ ) and (b) anisotropic ( $\alpha = 0.95$ ) TLAF. Irrespective of the presence of anisotropy, the bimagnon and trimagnon intensity complement each other at the zone center and at the zone boundary. Introduction of anisotropy removes the singularity due to the opening up of a gap in the spin-wave spectrum.

before undergoing an upward shift to  $6JS$  around the  $M$  point. In the presence of anisotropy [see Fig. 4(b)], there is an overall upward shift of the energy peak. The observed effect could be an artifact of considering a noninteracting trimagnon spectra. In the next section we consider the interacting bimagnon RIXS intensity up to  $1/S$  order.

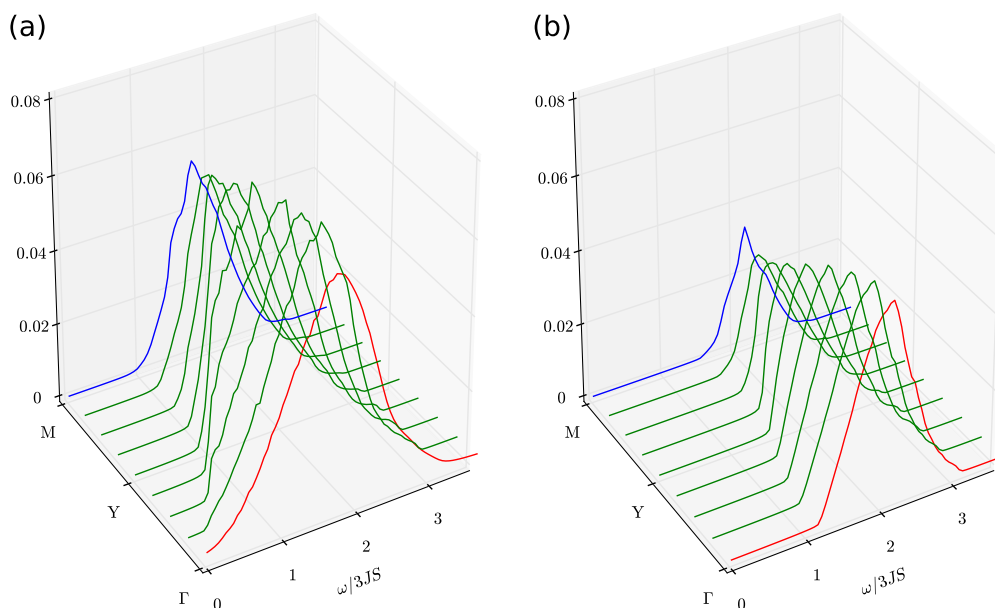


FIG. 4. (Color online) Pure trimagnon contribution to the RIXS intensity of the  $S = 1/2$  triangular-lattice antiferromagnet, (a) without anisotropy ( $\alpha = 1$ ) and (b) with anisotropy ( $\alpha = 0.95$ ).

### B. Bimagnon excitations: $1/S$ corrections

We now proceed with the analysis of the  $1/S$  correction to the two-magnon Green's function by taking into account both the self-energy correction to the single-magnon propagator  $G$  according to the Dyson equation and the vertex insertions to the two-magnon propagator  $\Pi$  which satisfies the Bethe-Salpeter (BS) equation [65,66]. The diagrammatic representation of such a procedure is depicted in Figs. 5(a) and 5(b). The total irreducible bimagnon scattering vertices in Fig. 5(c) fall into two categories, which we call *direct* ( $\mathcal{V}_4$ ) and *indirect* ( $\mathcal{V}_3^{a-d}$ ).

The direct collision between the two main magnons is caused by the quartic vertex  $\mathcal{V}_4$ , while the cubic vertices  $\mathcal{V}_3^{a-d}$  represent the indirect magnon-magnon interactions. Note that in the direct ladder interaction events the two main magnons created in the RIXS process are stable, while virtual decays and recombination are allowed in the indirect collision process. Using Feynman rules in momentum space then yields the following equations for the two-particle propagator and the vertex function:

$$\Pi_{\mathbf{k}\mathbf{k}'}(\mathbf{q}, \omega) = 2i \int \frac{d\omega'}{2\pi} G_{\mathbf{k}+\mathbf{q}}(\omega + \omega') G_{-\mathbf{k}}(-\omega') \Gamma_{\mathbf{k}\mathbf{k}'}(\omega, \omega'), \quad (23)$$

$$\Gamma_{\mathbf{k}\mathbf{k}'}(\omega, \omega') = \delta_{\mathbf{k}\mathbf{k}'} + \sum_{\mathbf{k}_1} 2i \int \frac{d\omega_1}{2\pi} G_{\mathbf{k}_1+\mathbf{q}}(\omega + \omega_1) G_{-\mathbf{k}_1}(-\omega_1) \times \mathcal{V}_{\mathbf{k}\mathbf{k}_1}^{\text{IR}}(\omega', \omega_1) \Gamma_{\mathbf{k}_1\mathbf{k}'}(\omega, \omega_1), \quad (24)$$

with the basic one-magnon propagator up to  $1/S$  order defined as

$$G^{-1}(\mathbf{k}, \omega) = \omega - \omega_{\mathbf{k}} + i0^+. \quad (25)$$

The factor of 2 in Eq. (23) and Eq. (24) stems from the two sets of contributions differing by the interchange of dummy momenta  $\mathbf{k}(\mathbf{k}_1) + \mathbf{q}$  and  $-\mathbf{k}(\mathbf{k}_1)$  according to the Wick's theorem. The lowest order two-particle irreducible interaction

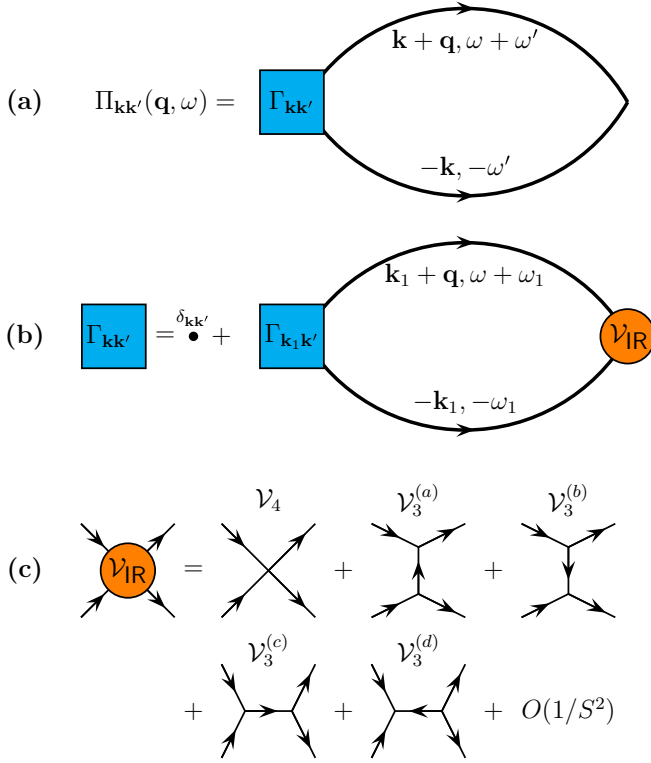


FIG. 5. (Color online) Diagrammatic representation for (a) a two-magnon propagator  $\Pi_{\mathbf{k}\mathbf{k}'}(\mathbf{q}, \omega)$ , (b) the Bethe-Salpeter equation of the vertex function  $\Gamma_{\mathbf{k}\mathbf{k}'}(\omega, \omega')$ , and (c) the  $1/S$ -order irreducible interaction  $\mathcal{V}_{\text{IR}}$ . Solid lines with an arrow in (a) and (b) stand for the single-magnon propagators.

vertices  $\mathcal{V}_{\text{IR}}$ , shown in Fig. 5(c), read as

$$\mathcal{V}_{\text{IR}} = \mathcal{V}_4 + \mathcal{V}_3^{(a)} + \mathcal{V}_3^{(b)} + \mathcal{V}_3^{(c)} + \mathcal{V}_3^{(d)}, \quad (26)$$

where the frequency-independent four-point vertex  $\mathcal{V}_4$  coming from the quartic Hamiltonian has the form

$$\mathcal{V}_4 = V_c(\mathbf{k}_1 + \mathbf{q}, -\mathbf{k}_1; \mathbf{k} + \mathbf{q}, -\mathbf{k}), \quad (27)$$

and the other four vertices  $\mathcal{V}_3^{(a-d)}$  in the same  $1/S$  order which are assembled from two three-point vertices and one frequency-dependent propagator can be written as

$$\begin{aligned} \mathcal{V}_3^{(a)} &= \frac{1}{(2!)^2} [V_a(\mathbf{k}_1 + \mathbf{q}, \mathbf{k} - \mathbf{k}_1; \mathbf{k} + \mathbf{q}) G_0(\mathbf{k} - \mathbf{k}_1, \omega' - \omega_1) \\ &\quad \times V_a^*(-\mathbf{k}, \mathbf{k} - \mathbf{k}_1; -\mathbf{k}_1)], \end{aligned} \quad (28)$$

$$\begin{aligned} \mathcal{V}_3^{(b)} &= \frac{1}{(2!)^2} [V_a^*(\mathbf{k} + \mathbf{q}, \mathbf{k}_1 - \mathbf{k}; \mathbf{k}_1 + \mathbf{q}) G_0(\mathbf{k}_1 - \mathbf{k}, \omega_1 - \omega') \\ &\quad \times V_a(-\mathbf{k}_1, \mathbf{k}_1 - \mathbf{k}; -\mathbf{k})], \end{aligned} \quad (29)$$

$$\begin{aligned} \mathcal{V}_3^{(c)} &= \frac{1}{(2!)^2} [V_a(\mathbf{k}_1 + \mathbf{q}, -\mathbf{k}_1; \mathbf{q}) G_0(\mathbf{q}, \omega) \\ &\quad \times V_a^*(\mathbf{k} + \mathbf{q}, -\mathbf{k}; \mathbf{q})], \end{aligned} \quad (30)$$

$$\begin{aligned} \mathcal{V}_3^{(d)} &= \frac{1}{(3!)^2} [V_b(\mathbf{k}_1 + \mathbf{q}, -\mathbf{k}_1, \mathbf{q}) G_0(-\mathbf{q}, -\omega) \\ &\quad \times V_b^*(\mathbf{k} + \mathbf{q}, -\mathbf{k}, \mathbf{q})], \end{aligned} \quad (31)$$

where we have retained only the bare propagator  $G_0$  for each intermediate line in  $\mathcal{V}_3^{(a-d)}$  in the spirit of  $1/S$  ranking. We further assume that two on-shell magnons are created and annihilated in the repeated ladder scattering process with  $\omega' \approx -\varepsilon_{\mathbf{k}}$  and  $\omega_1 \approx -\varepsilon_{\mathbf{k}_1}$  [52,53]. This approximation is best for sharp spectral peaks of the two main magnons in the scattering process where all the lowest-order irreducible vertices are not explicitly frequency dependent. Based on the above simplifications, we now derive the final solution of the interacting RIXS intensity from the ladder approximation BS equation.

An approach to solving the coupled BS equations is to decompose the irreducible vertices into lattice harmonics as demonstrated for the case of collinear antiferromagnet [38,40]. An inspection of the interaction vertices for the TLAf reveals that  $\mathcal{V}_3^{(a,b)}$  cannot be separated into the finite sum of products of the triangular-lattice harmonics; thus Eq. (14) cannot be algebraically solved in terms of a finite number of scattering channels. However, a numerical solution can be performed on finite lattices by summing over  $N$  points of  $\mathbf{k}$  in the first BZ, leading to a  $N \times N$  system for the linear solver. We adopt this numerical approach to compute the interacting intensity plots.

We begin with substituting (23) and (24) into (14),

$$\chi_2 = \sum_{\mathbf{k}\mathbf{k}'} M_{\mathbf{k}} M_{\mathbf{k}'} \left[ \delta_{\mathbf{k}\mathbf{k}'} \Pi_{\mathbf{k}} + \Pi_{\mathbf{k}} \sum_{\mathbf{k}_1} V_{\mathbf{k}\mathbf{k}_1} \Pi_{\mathbf{k}_1\mathbf{k}'} \right], \quad (32)$$

where  $\Pi_{\mathbf{k}} = 2[\omega - \varepsilon_{\mathbf{k}+\mathbf{q}} - \varepsilon_{\mathbf{k}} + i0^+]^{-1}$  represents the renormalized two-magnon propagator in the absence of vertex correction. The BZ on finite lattices can be divided into  $\sqrt{N} \times \sqrt{N}$  meshes with the replacement of the continuous momenta  $(\mathbf{k}, \mathbf{k}', \mathbf{k}_1)$  by discrete variables  $(m, n, l)$ . The elements for the bimagnon susceptibility matrix are given by

$$\hat{\chi}_{mn} = M_m M_n \left[ \delta_{mn} \Pi_m + \Pi_m \sum_l V_{ml} \Pi_{ln} \right]. \quad (33)$$

We then obtain the eigenvalue equation for these discrete momenta,

$$\mathcal{A}_{mn} = \mathcal{G}_{mn} + \sum_l \Gamma_{ml} \mathcal{A}_{ln}, \quad (34)$$

where the new functions are defined as

$$\mathcal{A}_{mn} = \hat{\Pi}_{mn} M_n, \quad \mathcal{G}_{mn} = \delta_{mn} \Pi_m M_n, \quad \Gamma_{ml} = \Pi_m V_{ml}. \quad (35)$$

A direct solution of (34) gives the final form of the  $\hat{\chi}$  matrix as

$$\hat{\chi} = \hat{\mathcal{D}}[\hat{\mathbf{I}} - \hat{\Gamma}]^{-1} \hat{\mathcal{G}}, \quad (36)$$

where all the matrices in Eq. (36) have  $N \times N$  dimensions with the matrix elements explicitly defined as

$$\hat{\mathbf{I}}_{mn} = \delta_{mn}, \quad \hat{\mathcal{D}}_{mn} = \delta_{mn} M_m, \quad (37)$$

$$\hat{\Gamma}_{mn} = \Pi_m V_{mn}, \quad \hat{\mathcal{G}}_{mn} = \delta_{mn} \Pi_m M_n. \quad (38)$$

The interacting pure bimagnon RIXS susceptibility can then be computed as

$$\chi_2(\mathbf{q}, \omega) = \sum_{m,n} \hat{\chi}_{mn}. \quad (39)$$

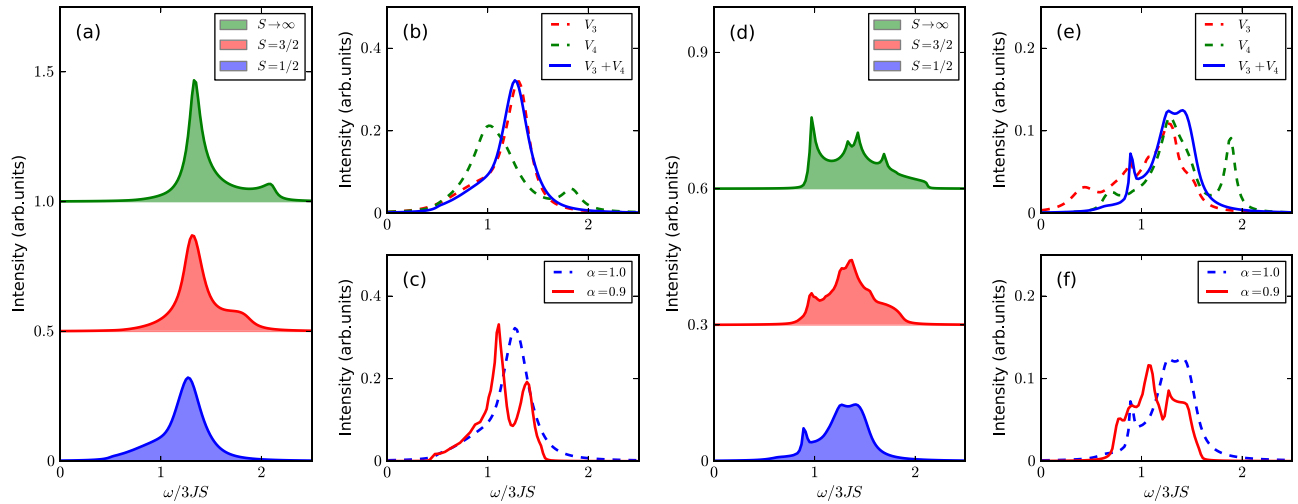


FIG. 6. (Color online) Interacting bimagnon RIXS intensity for (a)–(c) transformed momenta  $\mathbf{q} = M$  and (d)–(f)  $\mathbf{q} = Y$ . In (a) and (d) the evolution of the interacting bimagnon intensity profile with increasing spin value  $S$  for the isotropic model is shown. In (a) and (d),  $S \rightarrow \infty$  (top frame),  $S = 3/2$  (middle frame), and  $S = 1/2$  (bottom frame). In (b) and (e) comparisons of the contribution from the direct ( $\mathcal{V}_4$ ), indirect ( $\mathcal{V}_3$ ), and full ( $\mathcal{V}_3 + \mathcal{V}_4$ ) vertex corrections to the RIXS spectrum for  $S = 1/2$  and  $\alpha = 1$  are displayed. In (c) and (f) the effects of easy-plane anisotropy on the splitting feature of the interacting bimagnon spectrum are shown.

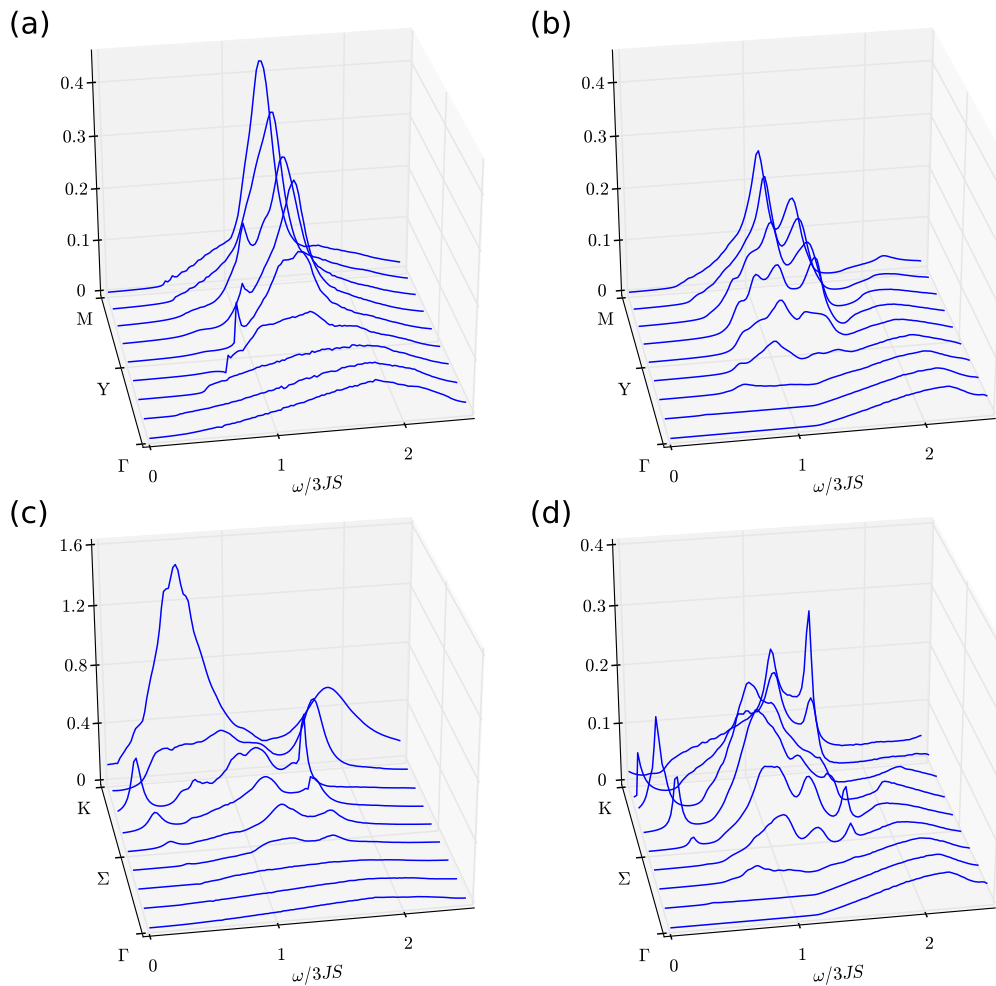


FIG. 7. (Color online) Full indirect RIXS spectra  $I_2 + I_3$  of the  $S = 1/2$   $XXZ$  triangular-lattice antiferromagnet with (a) and (c)  $\alpha = 1$  and (b) and (d)  $\alpha = 0.9$ , along the high-symmetry path  $\Gamma \rightarrow M$  and  $\Gamma \rightarrow K$  in the BZ.

In Fig. 6 we plot the results for interacting bimagnon RIXS intensity. We choose two special BZ momenta values,  $M$  and  $Y$ , to illustrate our findings. In Figs. 6(a) and 6(d) we show the progression of the indirect RIXS spectra shape as the spin  $S$  value is changed from the classical case  $S \rightarrow \infty$  (top) to  $S = 3/2$  (middle) to the maximal quantum case of  $S = 1/2$  (bottom). While the classical RIXS spectra from both momenta contain peaks due to the presence of Van Hove singularities, introduction of quantum fluctuations causes some of these spurious peaks to disappear. But observe that in the  $S = 1/2$  case the spectra shape is strikingly different. In the absence of anisotropy at the  $\mathbf{q} = M$  (roton transfer momentum), we observe a single peak at an energy of  $4JS$ . However, at the  $\mathbf{q} = Y$  point there is a multipeak structure [see Fig. 6(d)]. Now comparing the appearance of a single- or multipeak structure with the magnon decay intensity map [Fig. 1(b)], it is evident that there is a direct correlation between the stability of spin wave modes and peak splitting. The above-mentioned comparison is not restricted to these two chosen points. The

RIXS spectra generated from other special high-symmetry momentum transfer points also have the same features (see Fig. 7). Based on these observations, we propose that RIXS can be used as a probe to detect the presence of the roton mode in a TLAf. Furthermore, to provide a comprehensive picture of the effects of geometrical frustration and anisotropy we introduce a small anisotropy  $\alpha = 0.9$  in the system. From Figs. 6(c) and 6(f) it is clear that inclusion of anisotropy causes further peak splitting. Thus a proper explanation of the RIXS spectra features in a TLAf involves analyzing the effects of both magnon damping and anisotropy.

It is worth noting that the  $\mathcal{V}_4$  and  $\mathcal{V}_3$  vertices play an important role in the generation of the interacting bimagnon spectra. Especially at the roton point, including only the direct collision vertex does not renormalize the single-peak structure in the extreme quantum condition with  $S = 1/2$  [Fig. 6(b)]. The major contribution to the interacting RIXS spectra originates from the indirect vertices arising from the three-magnon interaction terms. This indicates that renormalization of the

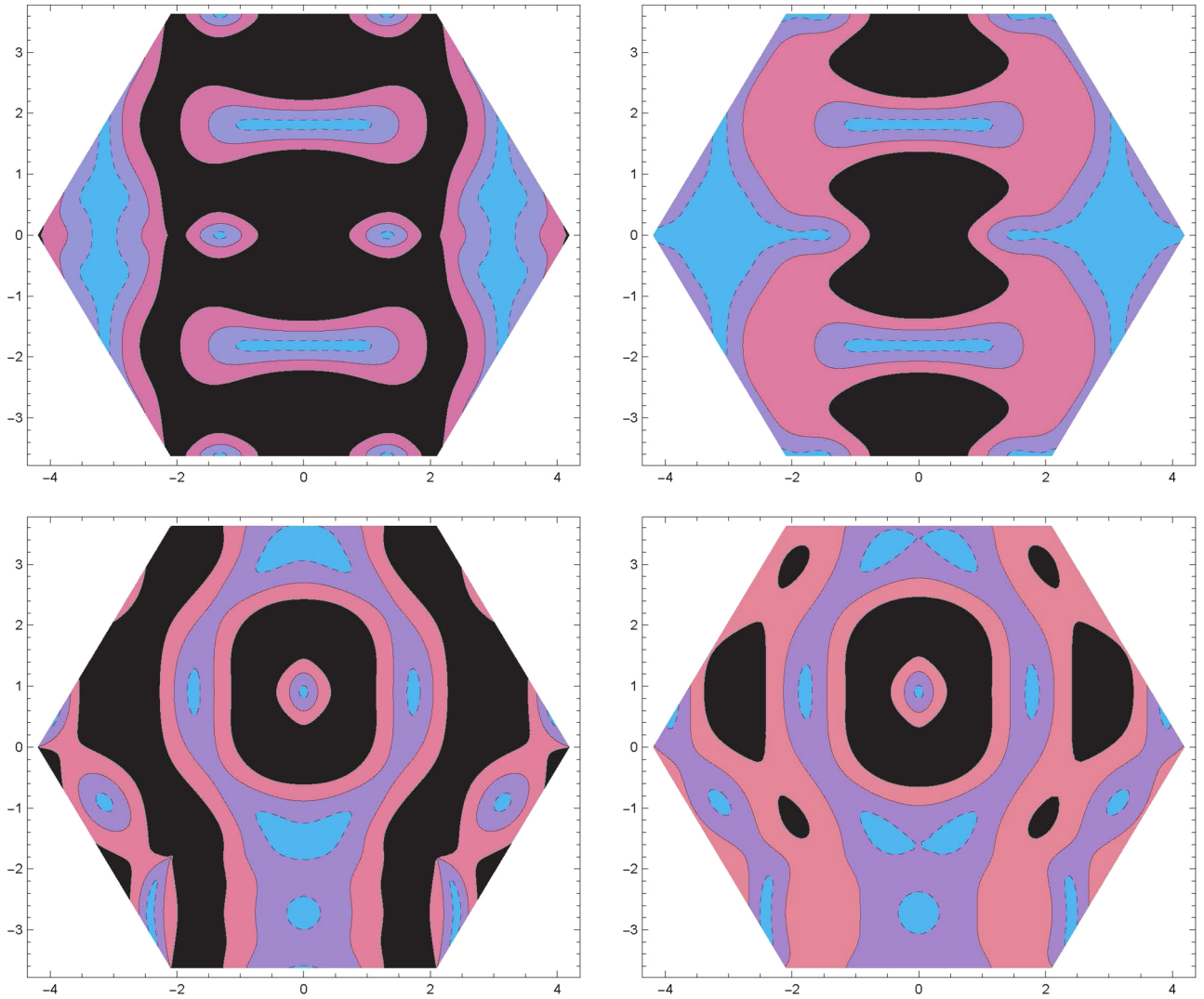


FIG. 8. (Color online) Contour plot of the bimagnon velocity in the first BZ of TLAf for (top) transferred momenta  $\mathbf{q} = M$  and (bottom)  $\mathbf{q} = Y$ . The first column is the bimagnon velocity in the absence of anisotropy ( $\alpha = 1$ ). The second column shows the anisotropic ( $\alpha = 0.9$ ) case. The lowest velocity contours are indicated by blue and pink bands. Relatively higher velocities are indicated by black regions. The prevalence of slow-moving bimagnon regions in the presence of anisotropy is an indicator of a multipeak RIXS structure.

spectrum at the roton point is due to the indirect  $\mathcal{V}_3$  vertices which involve virtual decay and recombination of the two main magnons in the scattering process. This is different from the  $\mathbf{q} = Y$  point where both the  $\mathcal{V}_4$  and  $\mathcal{V}_3$  vertices contribute, as seen in Fig. 6(e).

Before we end this section it is also important to point out an important difference between a Raman scattering calculation and RIXS. In the case of RIXS, the contributions of diagrams  $\mathcal{V}_3^{(c)}$  and  $\mathcal{V}_3^{(d)}$  vanish identically when the transferred momenta belong to the  $\Gamma$ - $M$  path or related symmetrical lines in the BZ in accordance with the magnetic Raman scattering study for which  $\mathbf{q} = 0$  [52]. To demonstrate this fact we consider the contributions of the two-particle irreducible vertices  $\mathcal{V}_3^{(c)}$  and  $\mathcal{V}_3^{(d)}$ , which are already in separated forms as functions of  $\mathbf{k}$  and  $\mathbf{k}'$ . The corresponding reducible vertex function (24) with respect to these diagrams can be directly obtained as

$$\Gamma_{\mathbf{k}\mathbf{k}'} = \delta_{\mathbf{k}\mathbf{k}'} + V_{a(b)}^*(\mathbf{k})f(\mathbf{q},\omega), \quad (40)$$

where  $f(\mathbf{q},\omega)$  is a function of only  $\omega$  and  $\mathbf{q}$ . Barring the noninteracting contributions, the vertex correction to the RIXS susceptibility is given by

$$\begin{aligned} \chi_V(\mathbf{q},\omega) &= f(\mathbf{q},\omega) \sum_{\mathbf{k}'} M_{\mathbf{k}'} \sum_{\mathbf{k}} M_{\mathbf{k}} \Pi_{\mathbf{k}} V_{a(b)}^*(\mathbf{k}) \\ &= \text{const} \times \sum_{\mathbf{k}} M_{\mathbf{k}} \Pi_{\mathbf{k}} V_{a(b)}^*(\mathbf{k}). \end{aligned} \quad (41)$$

In the above both  $M_{\mathbf{k}}$  and  $\Pi_{\mathbf{k}}$  are even functions of  $\mathbf{k}$ , while the function  $V_{a(b)}^*(\mathbf{k}) = V_{a(b)}^*(\mathbf{k} + \mathbf{q}, -\mathbf{k}, \mathbf{q})$  is an odd function with respect to  $\mathbf{k}$  when momentum  $\mathbf{q}$  is along the  $\Gamma$ - $M$  line (e.g.,  $q_x = 0$ ). Thus by virtue of the rotational symmetry of hexagonal lattices we can conclude that the total contributions of diagrams  $\mathcal{V}_3^{(c)}$  and  $\mathcal{V}_3^{(d)}$  vanish identically when transformed momenta  $\mathbf{q}$  are located in the lines from the center of the BZ to the middle of the BZ boundary. This implies that the simultaneous decay and source processes of the two main

magnons are prohibited in the repeated ladder scattering events when transferred momenta are along these symmetrical paths.

### C. Total RIXS intensity

Using Eq. (13), we compute the full indirect RIXS spectra up to  $1/S$  order. In Fig. 7 we display the RIXS line plots along the  $\Gamma \rightarrow M$  path and along the  $\Gamma \rightarrow K$  path. The features observed are reminiscent of those discussed for the noninteracting trimagnon spectra and the full interacting bimagnon spectra. As noted earlier, we find that at the  $\Gamma$  point the spectra originate purely from the trimagnon contribution, irrespective of the presence or absence of anisotropy. However, inclusion of anisotropy causes a downshift of the bimagnon contribution and an upward shift of the trimagnon spectra. Anisotropy gives rise to further splitting in the bimagnon case; however, the trimagnon spectra are not affected. The occurrence of peak splitting observed in the RIXS spectrum can be predicted by observing the bimagnon velocity plot. In a previous publication on the square-lattice Heisenberg magnet [40] we highlighted the connection between bimagnon velocity and the appearance of a multipeak structure in the RIXS spectra. Interestingly enough, even within the context of a TLAf, this relationship persists. To demonstrate this correlation, in Fig. 8, we show the bimagnon velocity intensity plot in both the presence and absence of anisotropy for the  $\mathbf{q} = M$  and the  $\mathbf{q} = Y$  points. The black regions represent the fastest-moving bimagnon velocities, which clearly disappear with the inclusion of anisotropy. As more puddles of slow-moving bimagnon velocity appear, so does the multipeak structure, as shown in Fig. 7. At the  $\mathbf{q} = M$  point the single roton peak melts away with increasing anisotropy, which comes along with low bimagnon velocity. A similar effect is observed at the  $\mathbf{q} = Y$  point, where with increasing anisotropy there are greater pockets of slow moving bimagnon. Hence, with anisotropy the peak splits further at  $Y$  point. Finally, in Fig. 9 we present the expected constant- $\omega$  scans of the total interacting RIXS intensity for four selected energies from low

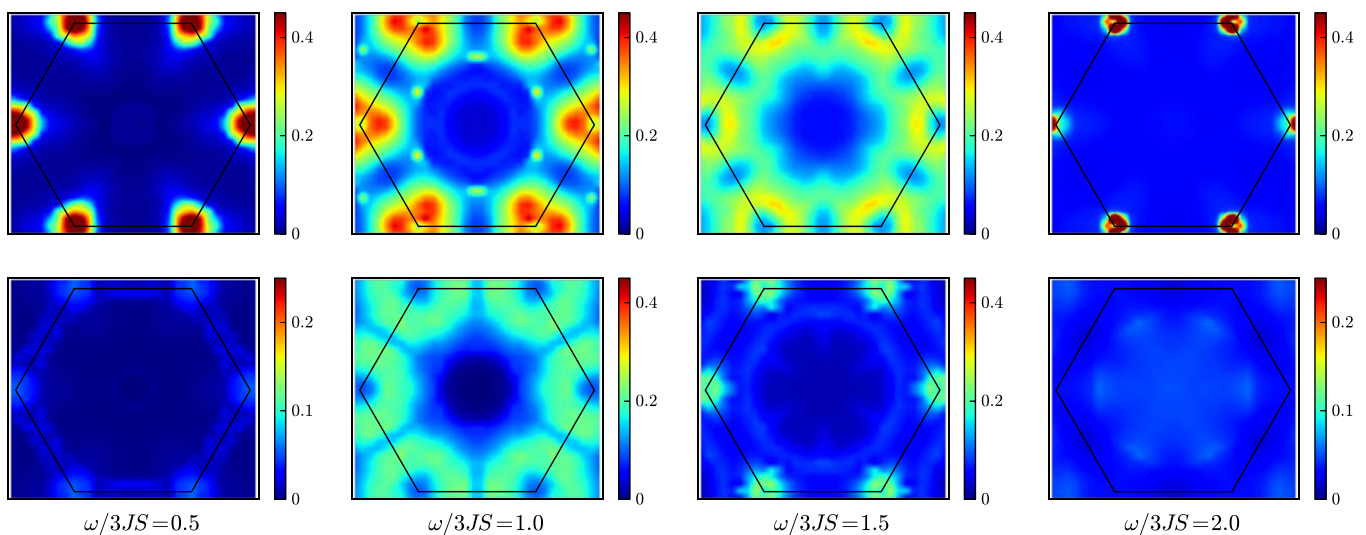


FIG. 9. (Color online) Intensity plots of the constant- $\omega$  scans of the full RIXS intensity  $I(\mathbf{q},\omega)$  scaled by  $(3JS)^2$  for the  $S = 1/2$   $XXZ$  triangular-lattice antiferromagnet in the  $\mathbf{q}$  plane with (top)  $\alpha = 1$  and (bottom)  $\alpha = 0.9$  at four representative energies. The prominent peaks on the corners are strongly reduced in the presence of anisotropy, in qualitative agreement with the noninteracting total spectral weight.

energy to high energy. One of the advantages of these constant-energy scans, which is reminiscent of the INS experiments, is that prominent peak structures are easy to distinguish [62]. For the isotropic model the interacting RIXS intensity is strongly peaked on the corners of the hexagonal BZ at low and high energies, while these peaks disperse along the edges of the BZ at intermediate energies. However, the presence of  $XXZ$  anisotropy strongly reduces these prominent features, which is in qualitative agreement with the noninteracting total spectral weight shown in Fig. 3.

## V. CONCLUSION

At present, no theoretical guidance for experimentalists on how to analyze and interpret the RIXS spectra of an ordered phase in a geometrically frustrated quantum magnet exists. Although a proposal for detecting spin-chirality terms in triangular-lattice Mott insulators via RIXS has been put forward [67], there has been no analysis of the effect of geometrical frustration and anisotropy on the indirect RIXS spectra. In this paper, using a  $1/S$  expansion spin-wave theory involving Bethe-Salpeter corrections, we investigated the key signatures of noncollinear ground-state ordering in the indirect RIXS spectra of a TLAF. We conclude that in the absence of anisotropy the root cause of the multiplex structure is magnon decay. This mechanism is different from that of a square lattice in which strong frustrating farther-neighbor interactions and anisotropy are required to cause peak splitting (instability). In the Introduction we put forward a couple of questions: (a) How does the presence of an intrinsic damping affect the indirect  $K$ -edge RIXS spectra? (b) What role does the interplay between geometrical frustration and spin anisotropy have in the RIXS spectra? Based on our calculations, we conclude that magnon damping does affect the spectra, causing the RIXS peak to be either stable (no splitting) or unstable (splitting leading to multiplex) in the absence or presence of damping, respectively. Geometrical frustration introduces noncollinear ordering, which introduces magnon damping. The stability or instability of the ensuing magnon mode then dictates the appearance of a single- or multiplex structure. By comparing the  $K$ -edge RIXS intensity of the square-lattice case to that of the TLAF, we find that the RIXS intensity does not vanish at the  $\Gamma$  point or at the antiferromagnetic wave vector. At the  $\Gamma$  point, the bimagnon intensity is zero, and the single-peak spectrum results purely from the trimagnon contribution, approximately at an energy scale of  $6JS$ , corresponding to the three-magnon energy. This provides experimentalists with a means to detect purely trimagnon excitations at the  $K$  edge. Our proposed scheme for detecting trimagnon excitations is different from that put forward in the paper by Ament and van den Brink [45] since we are not considering the  $L$  edge. The single roton peak occurs at an energy of  $4JS$  and can be used as an experimental signature to detect roton modes in a TLAF. In conclusion, our theoretical investigation demonstrates that RIXS has the potential to probe and provide a comprehensive characterization of the microscopic properties of bimagnon and trimagnon excitations in the TLAF across the entire BZ, which is beyond the capabilities of traditional low-energy optical techniques [50–53].

## ACKNOWLEDGMENTS

T.D. acknowledges funding support from a Cottrell Research Corporation grant and the Georgia Regents University Small Grants program. C.L., Z.H., and D.X.Y. acknowledge support from the Ministry of Science and Technology of China (973 project: 2012CB821400), NSFC-11074310, NSFC-11275279, RFDPE-20110171110026, NCET-11-0547, National Supercomputer Center in Guangzhou, and Fundamental Research Funds for the Central Universities of China.

## APPENDIX A: DERIVATION OF INTERACTING SPIN-WAVE THEORY

We utilize the Holstein-Primakoff transformation to bosonize the local rotating Hamiltonian (1),

$$S_i^z = S - a_i^\dagger a_i, \quad S_i^- = a_i^\dagger \sqrt{2S - a_i^\dagger a_i}, \quad S_i^+ = (S_i^-)^\dagger, \quad (\text{A1})$$

with subsequent expansion of the square root to first order in  $a_i^\dagger a_i/2S$ . This is followed by a Fourier transformation. The Fourier-transformed Hamiltonian takes the form

$$\mathcal{H} = H_0 + H_2 + H_3 + H_4 + O(S^{-1}). \quad (\text{A2})$$

The first term corresponds to the classical energy, and the quadratic Hamiltonian reads

$$H_2 = \sum_{\mathbf{k}} \left[ A_{\mathbf{k}} a_{\mathbf{k}}^\dagger a_{\mathbf{k}} + \frac{1}{2} B_{\mathbf{k}} (a_{\mathbf{k}}^\dagger a_{-\mathbf{k}}^\dagger + a_{-\mathbf{k}} a_{\mathbf{k}}) \right],$$

$$A_{\mathbf{k}} = 3JS \left[ 1 + \left( \alpha - \frac{1}{2} \right) \gamma_{\mathbf{k}} \right], \quad B_{\mathbf{k}} = -3JS \left( \alpha + \frac{1}{2} \right) \gamma_{\mathbf{k}}, \quad (\text{A3})$$

with the structure factor  $\gamma_{\mathbf{k}}$  defined as

$$\gamma_{\mathbf{k}} = \frac{1}{3} \left( \cos k_x + 2 \cos \frac{k_x}{2} \cos \frac{\sqrt{3}}{2} k_y \right). \quad (\text{A4})$$

We then diagonalize the harmonic part  $H_2$  by the Bogoliubov transformation

$$a_{\mathbf{k}} = u_{\mathbf{k}} b_{\mathbf{k}} + v_{\mathbf{k}} b_{-\mathbf{k}}^\dagger, \quad (\text{A5})$$

with the parameters  $u_{\mathbf{k}}$  and  $v_{\mathbf{k}}$  defined as

$$u_{\mathbf{k}}^2, v_{\mathbf{k}}^2 = \frac{A_{\mathbf{k}} \pm \varepsilon_{\mathbf{k}}}{2\varepsilon_{\mathbf{k}}}, \quad u_{\mathbf{k}} v_{\mathbf{k}} = -\frac{B_{\mathbf{k}}}{2\varepsilon_{\mathbf{k}}}, \quad (\text{A6})$$

and the linear spin-wave theory dispersion given by

$$\varepsilon_{\mathbf{k}} = \sqrt{A_{\mathbf{k}}^2 - B_{\mathbf{k}}^2} = 3JS \varepsilon_{\mathbf{k}}, \quad (\text{A7})$$

where we have defined the dimensionless energy

$$\varepsilon_{\mathbf{k}} = \sqrt{(1 - \gamma_{\mathbf{k}})(1 + 2\gamma_{\mathbf{k}})}. \quad (\text{A8})$$

Performing the Bogoliubov transformations in the cubic interaction term  $H_3$ , we obtain

$$H_3 = \frac{1}{2!} \sum_{\mathbf{k}_1 + \mathbf{k}_2 = \mathbf{k}_3} V_a(\mathbf{k}_1, \mathbf{k}_2; \mathbf{k}_3) (b_{\mathbf{k}_1}^\dagger b_{\mathbf{k}_2}^\dagger b_{\mathbf{k}_3} + \text{H.c.})$$

$$+ \frac{1}{3!} \sum_{\mathbf{k}_1 + \mathbf{k}_2 + \mathbf{k}_3 = 0} V_b(\mathbf{k}_1, \mathbf{k}_2, \mathbf{k}_3) (b_{\mathbf{k}_1}^\dagger b_{\mathbf{k}_2}^\dagger b_{\mathbf{k}_3}^\dagger + \text{H.c.}). \quad (\text{A9})$$

The explicit forms for the three-boson interaction vertices are

$$V_a(1,2;3) = 3Ji\sqrt{\frac{3S}{2}}[\bar{\gamma}_1(u_1+v_1)(u_2u_3+v_2v_3) + \bar{\gamma}_2(u_2+v_2)(u_1u_3+v_1v_3) - \bar{\gamma}_3(u_3+v_3) \times (u_1v_2+v_1u_2)], \quad (\text{A10})$$

$$V_b(1,2,3) = 3Ji\sqrt{\frac{3S}{2}}[\bar{\gamma}_1(u_1+v_1)(u_2v_3+v_2u_3) + \bar{\gamma}_2(u_2+v_2)(u_1v_3+v_1u_3) + \bar{\gamma}_3(u_3+v_3) \times (u_1v_2+v_1u_2)], \quad (\text{A11})$$

where  $u_i$  and  $v_i$  are Bogoliubov parameters and the function  $\bar{\gamma}_{\mathbf{k}}$  is defined as

$$\bar{\gamma}_{\mathbf{k}} = \frac{1}{3}\left(\sin k_x - 2\sin\frac{k_x}{2}\cos\frac{\sqrt{3}}{2}k_y\right). \quad (\text{A12})$$

The three-boson vertices  $V_a$  and  $V_b$  in  $H_3$  describe the interaction between one- and two-magnon states and are called the decay and the source vertices, respectively.

To derive the explicit forms of the quartic interaction term  $H_4$ , it is convenient to introduce the following Hartree-Fock averages:

$$n = \langle a_i^\dagger a_i \rangle = \frac{1}{2}c_0 + \frac{2\alpha-1}{4}c_1 - \frac{1}{2}, \quad (\text{A13})$$

$$m = \langle a_i^\dagger a_j \rangle = \frac{1}{2}c_1 + \frac{2\alpha-1}{4}c_2, \quad (\text{A14})$$

$$\Delta = \langle a_i a_j \rangle = \frac{2\alpha+1}{4}c_2, \quad (\text{A15})$$

$$\delta = \langle a_i^2 \rangle = \frac{2\alpha+1}{4}c_1, \quad (\text{A16})$$

with the two-dimensional integrals

$$c_l = \sum_{\mathbf{k}} \frac{(\gamma_{\mathbf{k}})^l}{\epsilon_{\mathbf{k}}} \quad (l=0,1,2). \quad (\text{A17})$$

After the mean-field decoupling, the quartic part is decomposed as

$$H_4 = \delta H_0 + \delta H_2 + \tilde{H}_4. \quad (\text{A18})$$

The first term  $\delta H_0$  is the correction to the ground-state energy, and the quadratic parts reads

$$\delta H_2 = \sum_{\mathbf{k}} \left[ \delta A_{\mathbf{k}} a_{\mathbf{k}}^\dagger a_{\mathbf{k}} + \frac{1}{2} \delta B_{\mathbf{k}} (a_{\mathbf{k}}^\dagger a_{-\mathbf{k}}^\dagger + a_{-\mathbf{k}} a_{\mathbf{k}}) \right], \quad (\text{A19})$$

with

$$\begin{aligned} \delta A_{\mathbf{k}} &= \frac{3}{2}[(1+2\alpha)\Delta + (1-2\alpha)m - 2n] \\ &\quad + \frac{3}{4}[(1+2\alpha)\delta + 2(1-2\alpha)n - 4m]\gamma_{\mathbf{k}}, \\ \delta B_{\mathbf{k}} &= \frac{3}{4}[(1+2\alpha)m + (1-2\alpha)\Delta] \\ &\quad + \frac{3}{4}[(1-2\alpha)\delta + 2(+2\alpha)n - 4\Delta]\gamma_{\mathbf{k}}. \end{aligned} \quad (\text{A20})$$

We then obtain the Hartree-Fock correction to the harmonic spin-wave spectrum

$$\delta \epsilon_{\mathbf{k}} = (u_{\mathbf{k}}^2 + v_{\mathbf{k}}^2)\delta A_{\mathbf{k}} + 2u_{\mathbf{k}}v_{\mathbf{k}}\delta B_{\mathbf{k}}. \quad (\text{A21})$$

The normal-ordered term  $\tilde{H}_4$  describes the multiparticle interactions. Here we only display the explicit expression for the lowest-order irreducible two-particle scattering amplitude, which is relevant for our calculations as

$$\tilde{H}_4^{2-p} = \sum_{\mathbf{k}_1+\mathbf{k}_2=\mathbf{k}_3+\mathbf{k}_4} V_c(\mathbf{k}_1, \mathbf{k}_2; \mathbf{k}_3, \mathbf{k}_4) b_{\mathbf{k}_1}^\dagger b_{\mathbf{k}_2}^\dagger b_{\mathbf{k}_3} b_{\mathbf{k}_4}, \quad (\text{A22})$$

with the vertex function

$$\begin{aligned} V_c(1,2;3,4) &= \frac{3JS}{16S} \{ (2\alpha+1)(\gamma_1+\gamma_2+\gamma_4)(u_1u_2u_3v_4+v_1v_2v_3u_4) + (2\alpha+1)(\gamma_1+\gamma_2+\gamma_3)(u_1u_2v_3u_4+v_1v_2u_3v_4) \\ &\quad + (2\alpha+1)(\gamma_2+\gamma_3+\gamma_4)(u_1v_2u_3u_4+v_1u_2v_3v_4) + (2\alpha+1)(\gamma_1+\gamma_3+\gamma_4)(u_1v_2v_3v_4+v_1u_2u_3u_4) \\ &\quad - [2(\gamma_{1-3}+\gamma_{2-3}+\gamma_{1-4}+\gamma_{2-4}) + (2\alpha-1)(\gamma_1+\gamma_2+\gamma_3+\gamma_4)](u_1u_2u_3u_4+v_1v_2v_3v_4) \\ &\quad - [2(\gamma_{1+2}+\gamma_{3+4}+\gamma_{1-3}+\gamma_{2-4}) + (2\alpha-1)(\gamma_1+\gamma_2+\gamma_3+\gamma_4)](u_1v_2u_3v_4+v_1u_2v_3u_4) \\ &\quad - [2(\gamma_{1+2}+\gamma_{3+4}+\gamma_{1-4}+\gamma_{2-3}) + (2\alpha-1)(\gamma_1+\gamma_2+\gamma_3+\gamma_4)](u_1v_2v_3u_4+v_1u_2u_3v_4) \}. \end{aligned} \quad (\text{A23})$$

By collecting all these terms together, we finally obtain the effective interacting spin-wave Hamiltonian (2).

## APPENDIX B: EXACT VERSUS NUMERICAL SOLUTION TO THE BS EQUATION

To test the validity of our numerical method on finite lattices ( $N = 69 \times 69$ ), we adopt the exact solution approach to solving a BS equation outlined in Appendix B of Ref. [40]. We obtain a separated form for the four-point vertex  $\mathcal{V}_4$  for the Heisenberg model ( $\alpha = 1$ ) on a triangular lattice, which has the following expression:

$$\mathcal{V}_4(\mathbf{k}_1 + \mathbf{q}, -\mathbf{k}_1; \mathbf{k} + \mathbf{q}, -\mathbf{k}) = \sum_{m,n=1}^{28} v_m(\mathbf{k}) \hat{\Gamma}_{mn} v_n(\mathbf{k}_1). \quad (\text{B1})$$

The channels  $v_n(\mathbf{k})$  are defined in Table I with the matrix elements of  $\hat{\Gamma}$  denoted by

$$\hat{\Gamma} = \frac{3JS}{16S} \begin{pmatrix} \hat{S}_1 & \hat{T} \\ \hat{T} & \hat{S}_2 \end{pmatrix}, \quad (\text{B2})$$

where the blocks are given by

$$\hat{T} = \begin{pmatrix} 2 & 2\lambda & -\frac{2}{3}\phi & -\frac{2}{3}\phi & 0 & 0 & 0 & 0 & 0 & 0 & 0 & 0 & 0 & 1 \\ 2\lambda & 2 & -\frac{2}{3}\phi & -\frac{2}{3}\phi & 0 & 0 & 0 & 0 & 0 & 0 & 0 & 0 & 0 & 2 \\ -\frac{2}{3}\chi & 0 & 2\chi & 2\chi & 0 & 0 & 0 & 0 & 0 & 0 & 0 & 0 & -\frac{8}{3}\chi & 0 \\ 0 & -\frac{2}{3}\chi & 2\chi & 2\chi & 0 & 0 & 0 & 0 & 0 & 0 & 0 & 0 & 0 & -\frac{8}{3}\chi \\ 0 & 2\chi & -\frac{2}{3}\chi & -\frac{2}{3}\chi & 0 & 0 & 0 & 0 & 0 & 0 & 0 & 0 & 0 & 0 \\ 2\chi & 0 & -\frac{2}{3}\chi & -\frac{2}{3}\chi & 0 & 0 & 0 & 0 & 0 & 0 & 0 & 0 & 0 & 0 \\ \frac{2}{3}\mu & 0 & -2\mu & -2\mu & 0 & 0 & 0 & 0 & 0 & 0 & 0 & 0 & \frac{8}{3}\mu & 0 \\ 0 & \frac{2}{3}\mu & -2\mu & -2\mu & 0 & 0 & 0 & 0 & 0 & 0 & 0 & 0 & 0 & \frac{8}{3}\mu \\ 0 & -2\mu & \frac{2}{3}\mu & \frac{2}{3}\mu & 0 & 0 & 0 & 0 & 0 & 0 & 0 & 0 & 0 & 0 \\ -2\mu & 0 & \frac{2}{3}\mu & \frac{2}{3}\mu & 0 & 0 & 0 & 0 & 0 & 0 & 0 & 0 & 0 & 0 \\ \frac{2}{3}\nu & 0 & -2\nu & -2\nu & 0 & 0 & 0 & 0 & 0 & 0 & 0 & 0 & \frac{8}{3}\nu & 0 \\ 0 & \frac{2}{3}\nu & -2\nu & -2\nu & 0 & 0 & 0 & 0 & 0 & 0 & 0 & 0 & 0 & \frac{8}{3}\nu \\ 0 & -2\nu & \frac{2}{3}\nu & \frac{2}{3}\nu & 0 & 0 & 0 & 0 & 0 & 0 & 0 & 0 & 0 & 0 \\ -2\nu & 0 & \frac{2}{3}\nu & \frac{2}{3}\nu & 0 & 0 & 0 & 0 & 0 & 0 & 0 & 0 & 0 & 0 \end{pmatrix},$$

$$\hat{S}_1 = \begin{pmatrix} 0 & 0 & 0 & 0 & -\frac{1}{3}\theta & 0 & 1 & C_q^0 & \frac{1}{3}S_q^0 & 0 & 0 & -S_q^0 & -\frac{2}{3}\phi & 0 \\ 0 & 0 & 0 & 0 & 0 & -\frac{1}{3}\theta & C_q^0 & 1 & 0 & \frac{1}{3}S_q^0 & -S_q^0 & 0 & 0 & -\frac{2}{3}\phi \\ & -\frac{4}{3}\gamma_q & -4\gamma_q & \theta & \theta & -\frac{1}{3}\theta & -\frac{1}{3}\theta & -S_q^0 & -S_q^0 & \frac{1}{3}S_q^0 & \frac{1}{3}S_q^0 & 2\phi & 2\phi & \\ & & -\frac{4}{3}\gamma_q & \theta & \theta & -\frac{1}{3}\theta & -\frac{1}{3}\theta & -S_q^0 & -S_q^0 & \frac{1}{3}S_q^0 & \frac{1}{3}S_q^0 & 2\phi & 2\phi & \\ & & & -\frac{1}{3}\theta & 0 & 0 & 0 & \frac{4}{3}S_q^0 & 0 & 0 & 0 & 0 & 0 & 0 \\ & & & & -\frac{1}{3}\theta & 0 & 0 & 0 & \frac{4}{3}S_q^0 & 0 & 0 & 0 & 0 & 0 \\ & & & & & -\frac{4}{3} & 0 & 0 & 0 & 0 & \frac{4}{3}S_q^0 & 0 & 0 & 0 \\ & & & & & & -\frac{4}{3} & 0 & 0 & -\frac{4}{3} & 0 & 0 & 0 & 0 \\ & & & & & & & -\frac{1}{3}\vartheta & 0 & 0 & 0 & 0 & 0 & 0 \\ & & & & & & & & -\frac{1}{3}\vartheta & 0 & 0 & 0 & 0 & 0 \\ & & & & & & & & & -\frac{4}{3} & \frac{4}{3}C_q^0 & 0 & 0 & 0 \\ & & & & & & & & & & -\frac{4}{3} & 0 & 0 & 0 \\ & & & & & & & & & & & -\frac{8}{3}\phi & 0 & 0 \\ & & & & & & & & & & & & -\frac{8}{3}\phi & 0 \end{pmatrix},$$

$$\hat{S}_2 = \begin{pmatrix} -\frac{8}{3} & -\frac{8}{3}\lambda & 0 & 0 & 0 & -\frac{8}{3}\chi & 0 & 0 & 0 & \frac{8}{3}\lambda & 0 & 0 & 0 & \frac{8}{3}\nu \\ -\frac{8}{3} & 0 & 0 & -\frac{8}{3}\chi & 0 & 0 & 0 & 0 & \frac{8}{3}\mu & 0 & 0 & 0 & \frac{8}{3}\nu & 0 \\ & -\frac{8}{3}\theta & 0 & 0 & 0 & -\frac{8}{3}\nu & 0 & 0 & 0 & 0 & -\frac{8}{3}\mu & 0 & 0 & 0 \\ & & -\frac{8}{3}\theta & 0 & 0 & 0 & -\frac{8}{3}\nu & 0 & 0 & 0 & 0 & -\frac{8}{3}\mu & 0 & 0 \\ & & & -\frac{8}{3} & -\frac{8}{3}\lambda & 0 & 0 & 0 & -\frac{8}{3}\nu & 0 & 0 & 0 & -\frac{8}{3}\mu & 0 \\ & & & & -\frac{8}{3} & 0 & 0 & -\frac{8}{3}\nu & 0 & 0 & 0 & 0 & -\frac{8}{3}\mu & 0 \\ & & & & & \frac{8}{3}\phi & 0 & 0 & 0 & -\frac{8}{3}\chi & 0 & 0 & 0 & 0 \\ & & & & & & \frac{8}{3}\phi & 0 & 0 & 0 & -\frac{8}{3}\chi & 0 & 0 & 0 \\ & & & & & & & -\frac{8}{3} & -\frac{8}{3}\lambda & 0 & 0 & 0 & -\frac{8}{3}\chi & 0 \\ & & & & & & & & -\frac{8}{3} & 0 & 0 & -\frac{8}{3}\chi & 0 & 0 \\ & & & & & & & & & \frac{8}{3}\phi & 0 & 0 & 0 & 0 \\ & & & & & & & & & & \frac{8}{3}\phi & 0 & 0 & 0 \\ & & & & & & & & & & & -\frac{8}{3} & \frac{8}{3}\lambda & -\frac{8}{3} \end{pmatrix}.$$

TABLE I. Definition of the channels  $v_n(\mathbf{k})$ .

$n$	$v_n(\mathbf{k})$	$n$	$v_n(\mathbf{k})$
1	$u_{\mathbf{k}+\mathbf{q}}u_{\mathbf{k}}$	15	$u_{\mathbf{k}+\mathbf{q}}v_{\mathbf{k}} \cos k_x \cos \frac{\sqrt{3}}{2}k_y$
2	$v_{\mathbf{k}+\mathbf{q}}v_{\mathbf{k}}$	16	$v_{\mathbf{k}+\mathbf{q}}u_{\mathbf{k}} \cos k_x \cos \frac{\sqrt{3}}{2}k_y$
3	$u_{\mathbf{k}+\mathbf{q}}v_{\mathbf{k}}$	17	$u_{\mathbf{k}+\mathbf{q}}u_{\mathbf{k}} \sin k_x \sin \frac{\sqrt{3}}{2}k_y$
4	$v_{\mathbf{k}+\mathbf{q}}u_{\mathbf{k}}$	18	$v_{\mathbf{k}+\mathbf{q}}v_{\mathbf{k}} \sin k_x \sin \frac{\sqrt{3}}{2}k_y$
5	$u_{\mathbf{k}+\mathbf{q}}u_{\mathbf{k}} \cos k_x$	19	$u_{\mathbf{k}+\mathbf{q}}v_{\mathbf{k}} \sin k_x \sin \frac{\sqrt{3}}{2}k_y$
6	$v_{\mathbf{k}+\mathbf{q}}v_{\mathbf{k}} \cos k_x$	20	$v_{\mathbf{k}+\mathbf{q}}u_{\mathbf{k}} \sin k_x \sin \frac{\sqrt{3}}{2}k_y$
7	$u_{\mathbf{k}+\mathbf{q}}v_{\mathbf{k}} \cos k_x$	21	$u_{\mathbf{k}+\mathbf{q}}u_{\mathbf{k}} \cos k_x \sin \frac{\sqrt{3}}{2}k_y$
8	$v_{\mathbf{k}+\mathbf{q}}u_{\mathbf{k}} \cos k_x$	22	$v_{\mathbf{k}+\mathbf{q}}v_{\mathbf{k}} \cos k_x \sin \frac{\sqrt{3}}{2}k_y$
9	$u_{\mathbf{k}+\mathbf{q}}u_{\mathbf{k}} \sin k_x$	24	$u_{\mathbf{k}+\mathbf{q}}v_{\mathbf{k}} \cos k_x \sin \frac{\sqrt{3}}{2}k_y$
10	$v_{\mathbf{k}+\mathbf{q}}v_{\mathbf{k}} \sin k_x$	24	$v_{\mathbf{k}+\mathbf{q}}u_{\mathbf{k}} \cos k_x \sin \frac{\sqrt{3}}{2}k_y$
11	$u_{\mathbf{k}+\mathbf{q}}v_{\mathbf{k}} \sin k_x$	25	$u_{\mathbf{k}+\mathbf{q}}u_{\mathbf{k}} \sin k_x \cos \frac{\sqrt{3}}{2}k_y$
12	$v_{\mathbf{k}+\mathbf{q}}u_{\mathbf{k}} \sin k_x$	26	$v_{\mathbf{k}+\mathbf{q}}v_{\mathbf{k}} \sin k_x \cos \frac{\sqrt{3}}{2}k_y$
13	$u_{\mathbf{k}+\mathbf{q}}u_{\mathbf{k}} \cos k_x \cos \frac{\sqrt{3}}{2}k_y$	27	$u_{\mathbf{k}+\mathbf{q}}v_{\mathbf{k}} \sin k_x \cos \frac{\sqrt{3}}{2}k_y$
14	$v_{\mathbf{k}+\mathbf{q}}v_{\mathbf{k}} \cos k_x \cos \frac{\sqrt{3}}{2}k_y$	28	$v_{\mathbf{k}+\mathbf{q}}u_{\mathbf{k}} \sin k_x \cos \frac{\sqrt{3}}{2}k_y$

In the above we have introduced the following notations:

$$C_q^0 = \cos q_x, \quad C_q^1 = \cos \frac{q_x}{2}, \quad C_q^2 = \cos \frac{\sqrt{3}}{2}q_y, \quad (\text{B3})$$

$$S_q^0 = \cos q_x, \quad S_q^1 = \cos \frac{q_x}{2}, \quad S_q^2 = \cos \frac{\sqrt{3}}{2}q_y, \quad (\text{B4})$$

$$\lambda = C_q^1 C_q^2, \quad \mu = C_q^1 S_q^2, \quad \nu = S_q^1 C_q^2, \quad \chi = S_q^1 S_q^2, \quad (\text{B5})$$

$$\theta = C_q^0 + 1, \quad \vartheta = C_q^0 - 1, \quad (\text{B6})$$

$$\phi = C_q^1 C_q^2 + 1, \quad \varphi = C_q^1 C_q^2 - 1. \quad (\text{B7})$$

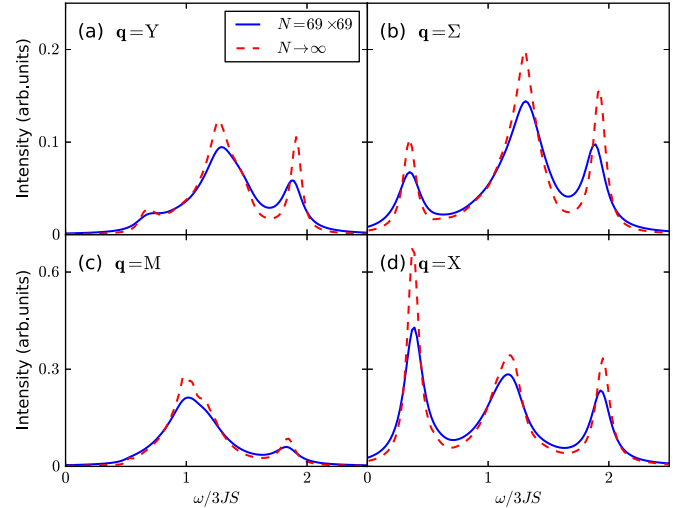


FIG. 10. (Color online) Interacting bimagnon RIXS intensity renormalized only by the direct interaction vertex  $\mathcal{V}_4$  based on the exact ( $N \rightarrow \infty$ ) vs numerical ( $N = 69 \times 69$ ) solution of the Bethe-Salpeter equation for a  $S = 1/2$  isotropic triangular-lattice antiferromagnet at various momenta in the BZ.

Only the upper right parts of  $\hat{S}_1$  and  $\hat{S}_2$  are shown since the matrices are symmetrical.

In Fig. 10 we show the results of our computation for  $S = 1/2$  and  $\alpha = 1$ . The numerical solution of Eq. (39) considering only the  $\mathcal{V}_4$  vertex is performed with  $69 \times 69$  lattice sites, while the integrals arising in the exact solution are solved on a mesh of size  $252 \times 252$  and then extrapolated to  $N \rightarrow \infty$  [40].

- [1] P. W. Anderson, Resonating valence bonds: A new kind of insulator? *Mater. Res. Bull.* **8**, 153 (1973).
- [2] Th. Jolicoeur and J. C. Le Guillou, Spin-wave results for the triangular Heisenberg antiferromagnet, *Phys. Rev. B* **40**, 2727 (1989).
- [3] Satoru J. Miyake, Spin-wave results for the staggered magnetization of triangular Heisenberg antiferromagnet, *J. Phys. Soc. Jpn.* **61**, 983 (1992).
- [4] A. V. Chubukov, S. Sachdev, and T. Senthil, Large- $s$  expansion for quantum antiferromagnets on a triangular lattice, *J. Phys.: Condens. Matter* **6**, 8891 (1994).
- [5] L. Capriotti, A. E. Trumper, and S. Sorella, Long-range Néel order in the triangular Heisenberg model, *Phys. Rev. Lett.* **82**, 3899 (1999).
- [6] W. Zheng, J. O. Fjærestad, R. R. P. Singh, R. H. McKenzie, and R. Coldea, Excitation spectra of the spin- $1/2$  triangular-lattice Heisenberg antiferromagnet, *Phys. Rev. B* **74**, 224420 (2006).
- [7] S. R. White and A. L. Chernyshev, Néel order in square and triangular lattice Heisenberg models, *Phys. Rev. Lett.* **99**, 127004 (2007).
- [8] P. H. Y. Li, R. F. Bishop, and C. E. Campbell, Quasiclassical magnetic order and its loss in a spin- $1/2$  Heisenberg antiferromagnet on a triangular lattice with competing bonds, *Phys. Rev. B* **91**, 014426 (2015).
- [9] D. A. Huse and V. Elser, Simple variational wave functions for two-dimensional Heisenberg spin- $1/2$  antiferromagnets, *Phys. Rev. Lett.* **60**, 2531 (1988).
- [10] B. Bernu, P. Lecheminant, C. Lhuillier, and L. Pierre, Exact spectra, spin susceptibilities, and order parameter of the quantum Heisenberg antiferromagnet on the triangular lattice, *Phys. Rev. B* **50**, 10048 (1994).
- [11] R. R. P. Singh and D. A. Huse, Three-sublattice order in triangular- and kagomé-lattice spin-half antiferromagnets, *Phys. Rev. Lett.* **68**, 1766 (1992).
- [12] Y. Shirata, H. Tanaka, A. Matsuo, and K. Kindo, Experimental realization of a spin- $1/2$  triangular-lattice Heisenberg antiferromagnet, *Phys. Rev. Lett.* **108**, 057205 (2012).
- [13] G. Koutroulakis, T. Zhou, Y. Kamiya, J. D. Thompson, H. D. Zhou, C. D. Batista, and S. E. Brown, Quantum phase diagram of the  $s = 1/2$  triangular-lattice antiferromagnet  $\text{Ba}_3\text{CoSb}_2\text{O}_9$ , *Phys. Rev. B* **91**, 024410 (2015).

- [14] T. Susuki, N. Kurita, T. Tanaka, H. Nojiri, A. Matsuo, K. Kindo, and H. Tanaka, Magnetization process and collective excitations in the  $s=1/2$  triangular-lattice Heisenberg antiferromagnet  $\text{Ba}_3\text{CoSb}_2\text{O}_9$ , *Phys. Rev. Lett.* **110**, 267201 (2013).
- [15] T. Ono, H. Tanaka, H. Aruga Katori, F. Ishikawa, H. Mitamura, and T. Goto, Magnetization plateau in the frustrated quantum spin system  $\text{Cs}_2\text{CuBr}_4$ , *Phys. Rev. B* **67**, 104431 (2003).
- [16] H. Kadowaki, K. Ubukoshi, K. Hirakawa, J. L. Martínez, and G. Shirane, Experimental study of new type phase transition in triangular lattice antiferromagnet  $\text{vcl}_2$ , *J. Phys. Soc. Jpn.* **56**, 4027 (1987).
- [17] R. Ishii, S. Tanaka, K. Onuma, Y. Nambu, M. Tokunaga, T. Sakakibara, N. Kawashima, Y. Maeno, C. Broholm, D. P. Gautreaux, J. Y. Chan, and S. Nakatsuji, Successive phase transitions and phase diagrams for the quasi-two-dimensional easy-axis triangular antiferromagnet  $\text{rb } 4 \text{ mn}(\text{moo } 4) 3$ , *Eur. Phys. Lett.* **94**, 17001 (2011).
- [18] M. Poienar, F. Damay, C. Martin, J. Robert, and S. Petit, Spin dynamics in the geometrically frustrated multiferroic  $\text{CuCrO}_2$ , *Phys. Rev. B* **81**, 104411 (2010).
- [19] S. Toth, B. Lake, S. A. J. Kimber, O. Pieper, M. Reehuis, A. T. M. N. Islam, O. Zaharko, C. Ritter, A. H. Hill, H. Ryll, K. Kiefer, D. N. Argyriou, and A. J. Williams,  $120^\circ$  helical magnetic order in the distorted triangular antiferromagnet  $\alpha\text{-Ca}_2\text{CuBr}_4$ , *Phys. Rev. B* **84**, 054452 (2011).
- [20] S. Toth, B. Lake, K. Hradil, T. Guidi, K. C. Rule, M. B. Stone, and A. T. M. N. Islam, Magnetic soft modes in the distorted triangular antiferromagnet  $\alpha\text{-Ca}_2\text{CuBr}_4$ , *Phys. Rev. Lett.* **109**, 127203 (2012).
- [21] R. Coldea, D. A. Tennant, A. M. Tsvelik, and Z. Tylczynski, Experimental realization of a 2d fractional quantum spin liquid, *Phys. Rev. Lett.* **86**, 1335 (2001).
- [22] R. Chen, H. Ju, H.-C. Jiang, O. A. Starykh, and L. Balents, Ground states of spin- $\frac{1}{2}$  triangular antiferromagnets in a magnetic field, *Phys. Rev. B* **87**, 165123 (2013).
- [23] B. Schmidt and P. Thalmeier, Quantum fluctuations in anisotropic triangular lattices with ferromagnetic and antiferromagnetic exchange, *Phys. Rev. B* **89**, 184402 (2014).
- [24] P. Hauke, T. Roscilde, V. Murg, J. I. Cirac, and R. Schmied, Modified spin-wave theory with ordering vector optimization: spatially anisotropic triangular lattice and  $j_1 j_2 j_3$  model with Heisenberg interactions, *New J. Phys.* **13**, 075017 (2011).
- [25] M. Kohno, O. A. Starykh, and L. Balents, Spinons and triplons in spatially anisotropic frustrated antiferromagnets, *Nat. Phys.* **3**, 790 (2007).
- [26] M. Swanson, J. T. Haraldsen, and R. S. Fishman, Critical anisotropies of a geometrically frustrated triangular-lattice antiferromagnet, *Phys. Rev. B* **79**, 184413 (2009).
- [27] R. S. Fishman and S. Okamoto, Noncollinear magnetic phases of a triangular-lattice antiferromagnet and of doped  $\text{CuFeO}_2$ , *Phys. Rev. B* **81**, 020402 (2010).
- [28] E. A. Ghioldi, A. Mezio, L. O. Manuel, R. R. P. Singh, J. Oitmaa, and A. E. Trumper, Magnons and excitation continuum in  $\text{xxz}$  triangular antiferromagnetic model: Application to  $\text{Ba}_3\text{CoSb}_2\text{O}_9$ , *Phys. Rev. B* **91**, 134423 (2015).
- [29] N. Suzuki, F. Matsubara, S. Fujiki, and T. Shirakura, Absence of classical long-range order in an  $s = \frac{1}{2}$  Heisenberg antiferromagnet on a triangular lattice, *Phys. Rev. B* **90**, 184414 (2014).
- [30] A. Weichselbaum and S. R. White, Incommensurate correlations in the anisotropic triangular Heisenberg lattice, *Phys. Rev. B* **84**, 245130 (2011).
- [31] P. Hauke, Quantum disorder in the spatially completely anisotropic triangular lattice, *Phys. Rev. B* **87**, 014415 (2013).
- [32] R. Coldea, S. M. Hayden, G. Aeppli, T. G. Perring, C. D. Frost, T. E. Mason, S.-W. Cheong, and Z. Fisk, Spin waves and electronic interactions in  $\text{La}_2\text{CuO}_4$ , *Phys. Rev. Lett.* **86**, 5377 (2001).
- [33] H. M. Rønnow, D. F. McMorrow, R. Coldea, A. Harrison, I. D. Youngson, T. G. Perring, G. Aeppli, O. Syljuåsen, K. Lefmann, and C. Rischel, Spin dynamics of the 2d spin  $\frac{1}{2}$  quantum antiferromagnet copper deuteroformate tetradeuterate (cfd), *Phys. Rev. Lett.* **87**, 037202 (2001).
- [34] L. J. P. Ament, M. van Veenendaal, T. P. Devereaux, J. P. Hill, and J. van den Brink, Resonant inelastic x-ray scattering studies of elementary excitations, *Rev. Mod. Phys.* **83**, 705 (2011).
- [35] J. P. Hill, G. Blumberg, Y.-J.e Kim, D. S. Ellis, S. Wakimoto, R. J. Birgeneau, S. Komiya, Y. Ando, B. Liang, R. L. Greene, D. Casa, and T. Gog, Observation of a 500 meV collective mode in  $\text{La}_{2-x}\text{Sr}_x\text{CuO}_4$  and  $\text{Nd}_2\text{CuO}_4$  using resonant inelastic x-ray scattering, *Phys. Rev. Lett.* **100**, 097001 (2008).
- [36] D. S. Ellis, Jungho Kim, J. P. Hill, S. Wakimoto, R. J. Birgeneau, Y. Shvyd'ko, D. Casa, T. Gog, K. Ishii, K. Ikeuchi, A. Paramakanti, and Y.-J. Kim, Magnetic nature of the 500 meV peak in  $\text{La}_{2-x}\text{Sr}_x\text{CuO}_4$  observed with resonant inelastic x-ray scattering at the Cu  $k$ -edge, *Phys. Rev. B* **81**, 085124 (2010).
- [37] J. van den Brink, The theory of indirect resonant inelastic x-ray scattering on magnons, *Europhys. Lett.* **80**, 47003 (2007).
- [38] T. Nagao and J.-I. Igarashi, Two-magnon excitations in resonant inelastic x-ray scattering from quantum Heisenberg antiferromagnets, *Phys. Rev. B* **75**, 214414 (2007).
- [39] F. Forte, L. J. P. Ament, and J. van den Brink, Magnetic excitations in  $\text{La}_2\text{CuO}_4$  probed by indirect resonant inelastic x-ray scattering, *Phys. Rev. B* **77**, 134428 (2008).
- [40] C. Luo, T. Datta, and D. X. Yao, Spectrum splitting of bimagnon excitations in a spatially frustrated Heisenberg antiferromagnet revealed by resonant inelastic x-ray scattering, *Phys. Rev. B* **89**, 165103 (2014).
- [41] C. J. Jia, C.-C. Chen, A. P. Sorini, B. Moritz, and T. P. Devereaux, Uncovering selective excitations using the resonant profile of indirect inelastic x-ray scattering in correlated materials: observing two-magnon scattering and relation to the dynamical structure factor, *New J. Phys.* **14**, 113038 (2012).
- [42] L. J. P. Ament, G. Ghiringhelli, M. Moretti Sala, L. Braicovich, and J. van den Brink, Theoretical demonstration of how the dispersion of magnetic excitations in cuprate compounds can be determined using resonant inelastic x-ray scattering, *Phys. Rev. Lett.* **103**, 117003 (2009).
- [43] M. W. Haverkort, Theory of resonant inelastic x-ray scattering by collective magnetic excitations, *Phys. Rev. Lett.* **105**, 167404 (2010).
- [44] C. J. Jia, E. A. Nowadnick, K. Wohlfeld, Y. F. Kung, C.-C. Chen, S. Johnston, T. Tohyama, B. Moritz, and T. P. Devereaux, Persistent spin excitations in doped antiferromagnets revealed by resonant inelastic light scattering, *Nat. Commun.* **5**, 3314 (2014).

- [45] L. J. P. Ament and J. van den Brink, Strong three-magnon scattering in cuprates by resonant x-rays, [arXiv:1002.3773](#).
- [46] M. E. Zhitomirsky and A. L. Chernyshev, Colloquium: Spontaneous magnon decays, *Rev. Mod. Phys.* **85**, 219 (2013).
- [47] A. L. Chernyshev and M. E. Zhitomirsky, Magnon decay in noncollinear quantum antiferromagnets, *Phys. Rev. Lett.* **97**, 207202 (2006).
- [48] J. van den Brink and M. van Veenendaal, Correlation functions measured by indirect resonant inelastic x-ray scattering, *Europhys. Lett.* **73**, 121 (2006).
- [49] L. J. P. Ament, F. Forte, and J. van den Brink, Ultrashort lifetime expansion for indirect resonant inelastic x-ray scattering, *Phys. Rev. B* **75**, 115118 (2007).
- [50] T. P. Devereaux and R. Hackl, Inelastic light scattering from correlated electrons, *Rev. Mod. Phys.* **79**, 175 (2007).
- [51] F. Vernay, T. P. Devereaux, and M. J. P. Gingras, Raman scattering for triangular lattices spin-1/2 Heisenberg antiferromagnets, *J. Phys.: Condens. Matter* **19**, 145243 (2007).
- [52] N. Perkins and W. Brenig, Raman scattering in a Heisenberg  $s = \frac{1}{2}$  antiferromagnet on the triangular lattice, *Phys. Rev. B* **77**, 174412 (2008).
- [53] N. B. Perkins, G.-W. Chern, and W. Brenig, Raman scattering in a Heisenberg  $s = \frac{1}{2}$  antiferromagnet on the anisotropic triangular lattice, *Phys. Rev. B* **87**, 174423 (2013).
- [54] W. Zheng, J. O. Fjærestad, R. R. P. Singh, R. H. McKenzie, and R. Coldea, Anomalous excitation spectra of frustrated quantum antiferromagnets, *Phys. Rev. Lett.* **96**, 057201 (2006).
- [55] O. A. Starykh, A. V. Chubukov, and A. G. Abanov, Flat spin-wave dispersion in a triangular antiferromagnet, *Phys. Rev. B* **74**, 180403 (2006).
- [56] A. L. Chernyshev and M. E. Zhitomirsky, Spin waves in a triangular lattice antiferromagnet: Decays, spectrum renormalization, and singularities, *Phys. Rev. B* **79**, 144416 (2009).
- [57] H. D. Zhou, Cenke Xu, A. M. Hallas, H. J. Silverstein, C. R. Wiebe, I. Umegaki, J. Q. Yan, T. P. Murphy, J.-H. Park, Y. Qiu, J. R. D. Copley, J. S. Gardner, and Y. Takano, Successive phase transitions and extended spin-excitation continuum in the  $s = \frac{1}{2}$  triangular-lattice antiferromagnet  $\text{Ba}_3\text{CoSb}_2\text{O}_9$ , *Phys. Rev. Lett.* **109**, 267206 (2012).
- [58] R. Coldea, D. A. Tennant, and Z. Tylczynski, Extended scattering continua characteristic of spin fractionalization in the two-dimensional frustrated quantum magnet  $\text{Cs}_2\text{CuCl}_4$  observed by neutron scattering, *Phys. Rev. B* **68**, 134424 (2003).
- [59] J. Oh, M. D. Le, J. Jeong, J.-h. Lee, H. Woo, W.-Y. Song, T. G. Perring, W. J. L. Buyers, S.-W. Cheong, and J.-G. Park, Magnon breakdown in a two dimensional triangular lattice Heisenberg antiferromagnet of multiferroic  $\text{LuMnO}_3$ , *Phys. Rev. Lett.* **111**, 257202 (2013).
- [60] M. Y. Veillette, A. J. A. James, and F. H. L. Essler, Spin dynamics of the quasi-two-dimensional spin- $\frac{1}{2}$  quantum magnet  $\text{Cs}_2\text{CuCl}_4$ , *Phys. Rev. B* **72**, 134429 (2005).
- [61] D. Dalidovich, R. Sknepnek, A. J. Berlinsky, J. Zhang, and C. Kallin, Spin structure factor of the frustrated quantum magnet  $\text{Cs}_2\text{CuCl}_4$ , *Phys. Rev. B* **73**, 184403 (2006).
- [62] M. Mourigal, W. T. Fuhrman, A. L. Chernyshev, and M. E. Zhitomirsky, Dynamical structure factor of the triangular-lattice antiferromagnet, *Phys. Rev. B* **88**, 094407 (2013).
- [63] C. M. Canali and Mats Wallin, Spin-spin correlation functions for the square-lattice Heisenberg antiferromagnet at zero temperature, *Phys. Rev. B* **48**, 3264 (1993).
- [64] J. Lorenzana, G. Seibold, and R. Coldea, Sum rules and missing spectral weight in magnetic neutron scattering in the cuprates, *Phys. Rev. B* **72**, 224511 (2005).
- [65] R. W. Davies, S. R. Chinn, and H. J. Zeiger, Spin-wave approach to two-magnon raman scattering in a simple antiferromagnet, *Phys. Rev. B* **4**, 992 (1971).
- [66] C. M. Canali and S. M. Girvin, Theory of raman scattering in layered cuprate materials, *Phys. Rev. B* **45**, 7127 (1992).
- [67] W.-H. Ko and P. A. Lee, Proposal for detecting spin-chirality terms in mott insulators via resonant inelastic x-ray scattering, *Phys. Rev. B* **84**, 125102 (2011).